A NEW METHOD TO ESTIMATE LIGHT ECHO APPARENT PROPER MOTION VECTORS

A NEW METHOD TO ESTIMATE LIGHT ECHO APPARENT PROPER MOTION VECTORS

By

Niloufar Javid Khalili

A Thesis Submitted to the School of Graduate Studies
in Partial Fulfilment of the Requirements
for the Degree
Master of Science

McMaster University

Master of Science (2016) McMaster University

(Physics and Astronomy) Hamilton, Ontario

TITLE:A New Method to Estimate Light Echo Apparent Proper Motion Vectors

AUTHOR: Niloufar Javid Khalili

SUPERVISOR: Professor Douglas Welch

NUMBER OF PAGES: xxii, 102

Abstract

This thesis presents a new method to estimate the Apparent Proper Motion (APM) vector and its uncertainty for supernova light echoes (LEs) and tests its usefulness in practice on LEs due to two old Galactic supernovae (SNe) - Cas A and Tycho. Ten instances of two-dimensional cross-correlation (2-D CC) of images containing light echoes at different epochs are employed to examine how well this new method works in practice. The images selected for this work originate from KPNO 4m Mosaic 1.1 images and were originally processed by the Pan-STARRS pipeline.

All the APM estimates reported in this thesis are within 1σ of estimates based on supernova distance and age provided reasonable inclinations are assumed. It was found that several factors tend to reduce the expected precision of this method and these include: 1) the existence of more than one LE feature for each epoch, 2) longer intervals between the two epochs lead to a bias, and 3) the existence of dust filaments at more than one depth along the line of sight. The results of three LE fields which were in common with the previous studies by Rest et al in 2008 and 2011, were compared and a good agreement was found between them in difference-images with the same time interval.

Since pixel values have a significant role in the introduced method, a control region is considered to eliminate the defect of the irrelevant residuals to the LE features. Hence, the introduced method was not straightforward. In addition, this method was not thoroughly manual independent, as the benefits of the visual measurement from the previous method reported by Rest et al. (2008) and (2011) were adopted for this method. However, compared to the previous manual technique, there were much less

manual measurements were taken for the whole LE features in one frame. Considering all the challenges, the CC method is favourable as the APM vector uncertainty can be determined, which has not been achievable with previous method before.

Keywords: Cas A, Tycho, supernovae, historical supernovae, light echoes, apparent proper motion.

Dedicated to my beloved

Iman

Acknowledgements

Having a different and fabulous experience out of my home country, Iran, made memorable moments for ever for me during spending my second master in my life at McMaster University. I would like to deeply thank the people who have supported and helped me so much over the passed span of my life. First, I would like to sincerely thank my supervisor, Professor Douglas Welch who supervised me with admirable patience and gracious advices. He has left positive impact on my attitude toward science especially toward observational astrophysics. I am grateful to have had honour and chance to study under supervision of such a brilliant and experienced supervisor. I would like to thank my thesis committee, Dr. Christine Wilson and Dr. Laura Parker. Your valuable advices inspired me a lot. I am also thankful to Dr. Armin Rest who generously gave us his group difference-images for this thesis.

Many thanks are due to Mara Esposto, Rosemary McNeice, Cheryl Johnston, and Tine Stewart, the staffs of the Department of Physics and Astronomy at McMaster University who always kindly helped and guided me with smiles on their faces. I have had a wonderful time with my office-mates and other friends in our department. I would like to say many thanks to all for their suggestions and helps. In particular, I owe so much to my friends Gandhali Joshi, Gwendolyn Eadie, and Meghan Miholics for help with editing. Without them, it would have been impossible to finish my thesis. I deeply thank Sahar Darvish-Molla who I met at McMaster by chance. Her spiritual supports and valuable advice have helped me a lot.

I have a kind, precious and invaluable family who always support me. My grandparents have had an important role in my life and in constructing my attitude toward life. I am so pleased and grateful to have you in my life. I love you very much. I want to

thank my sisters Solmaz and Neda and my brother Aidin who unconditionally love me and keep my heart warm. My parents have always motivated me to live differently and dedicated my life to science. I owe my life to them. Writing cannot express my feelings to you. Both of you have always nurtured me in my life and helped me step by step. I deeply and sincerely thank you, Nayereh and Ali, my kind and beautiful mother and father.

My lovely spouse, Iman! You have always been there for me, helped me and loved me unconditionally. You endlessly have taken my hands and walked with me in each moment of our life. I could not finish this stage of my life without your helps and supports. In dark and hopeless moments you were present and motivated me. I was so lucky to see you in the bus station on my way to work at the university, seven years ago. From that moment, my life has been colourful and warm. Iman, my best friend! I sincerely thank you for being with me and for all the beautiful moments that you have created for us.

Scientific Motivations

There are several reasons that motivate astronomers to study supernovae (SNe) and in particular inspire us to learn in greater detail about SNe scattered light echoes (LEs).

General Astrophysical Motivations

Supernovae (SNe) are important and influential events that affect our understanding in different areas of astrophysics. Knowing more about SNe outbursts in greater detail can reveal a wealth of important information about astrophysical issues and can lead to their solution. Astrophysical uses of SNe include using SNe as standard candles in observational cosmology, understanding nucleosynthesis from SNe remnants (SNRs), and understanding their role in cosmic ray acceleration.

Motivations for Studying LEs

Studying LEs is an important tool to investigate SNe outbursts. Discovering SNe LEs enabled astronomers to obtain the spectra of these transient events centuries later. Researchers have the rare opportunity to simultaneously study the remnant and the outburst. Additionally, investigating the outburst from different angles allows the asymmetry of the event to be estimated.

Specific Motivations for Improving LE Apparent Proper Motion Estimates

Armin Rest and his group pioneered the development and investigation of the theory of LEs. They used a reduction toolkit to understand the LE observations during their study. The researchers used a visual technique to estimate the apparent proper motion (APM) of LEs in order to estimate the age of the SN remnants (SNR).

Aims of This Thesis

Light echo APMs provide a number of pieces of useful information. However, the

manual technique employed prior to this work may be affected by selection biases and the uncertainties are difficult to establish and justify. The method explored in this work, using cross-correlation, use less manual input and provides more easily interpreted uncertainties in the LE APM vector.

List of Abbreviations

1-D: One-dimensional

2-D: Two-dimensional

2-D CC: Two-dimensional Cross-Correlation

APM: Apparent Proper Motion

CC: Cross Correlation

Cas A: Cassiopeia A

CCD: Charge Coupled Device

CCSN : Core-Collapse Supernovae

FITS: Flexible Image Transport System

FT: Fourier Transform

FOV: Field of View

FWHM: Full Width at Half Maximum

ISM: Interstellar Medium

IRAF: Image Reduction and Analysis Facility

KPNO: Kitt Peak National Observatory

LEs: Light Echoes

LMC: Large Magellanic Cloud

LoS: Line of Sight

MOSA: Mosaic-1.1 imager

MW: Milky Way

NOAO: National Optical Astronomy Observatories

NRMSD: Normalized Root-Mean-Square Deviation

NS: Neutron Star

PA: Position Angle

PI: Principal Investigator

Pan-STARRS: Panoramic Survey Telescope and Rapid Response System

PSF: Point Spread Function

RMSD: Root-Mean-Square Deviation

SuperMACHO: Super MAssive Compact Halo Object

SNe: Supernovae

SNRs : Supernova Remnants

WCS: World Coordinate System

WD: White Dwarf

Contents

List of Figures

List of Tables

Chapter 1

Introduction

The scattered light by interstellar dust filaments around transient luminous events such as supernovae (SNe) are called Light echoes (LEs). In this chapter, SNe are introduced, followed by their LE features, geometries, characteristics, and a review of previous studies in these areas. Finally, the observation materials and reduction technique will be reviewed, and in the last section, difference-imaging will be introduced.

1.1 Supernovae

Supernovae (SNe) are the violent end points of the evolution of some stars, in which very large amounts of material and energy are released into their surroundings (Stephenson & Green, 2002). This stellar explosion phenomenon involves collapse or disruption of the star. During the SN event, the luminosity of the explosion is comparable to that of the whole galaxy from which it originates and can outshine the galaxy entirely for a brief interval of time before fading from view over several weeks or even several months (Giacobbe, 2005).

This phenomenon had been known by different names such as 'giant novae' by Knut Lundmark (1920) and Heber D. Curtis (1921) separately, 'exceptional novae' by Hubble (1929), and 'Hauptnovae', which means 'chief novae' in German, by Baade (1929) between 1920 and 1933 (Osterbrock, 2001). Fritz Zwicky and Walter Baade introduced the term *supernovae* in seminars and an astrophysics course at Caltech in 1931. They were also the first to postulate that neutron stars could be formed from SNe in the abstract of their joint paper at an American Physical Society meeting at Stanford in December 1933 which was published in the Physical Review in early 1934 (Osterbrock, 2001). Now, we know that both neutron stars black holes can be formed during the collapse of a massive star during a SN (Roberts & Colbert, 2003).

1.1.1 Supernova Classification

Minkowskii (1941) classified SNe (Cappellaro & Turatto, 2001) according to the detection of hydrogen lines in their spectrum. This basic taxonomy was continued until the 1980s. In the mid-80s, the presence of the spectral lines of other elements generated sub-division of this classification (Gaskell et al., 1986).

Supernovae are the result of two formation routes: thermonuclear and core-collapse (Turatto, 2003). The progenitor of the thermonuclear SN types is supposed to be a binary system, of which at least one of the members is a white dwarf (WD) (Woosley, 1997) that accreted mass from its companion. The other companion is either a red giant (Whelan & Iben Jr, 1973; Iben Jr & Tutukov, 1984) or another WD (Iben Jr & Tutukov, 1984).

Core-collapse supernovae progenitors are young massive stars and they are found in star formation regions (Smartt, 2009; Smartt, Eldridge, Crockett, & Maund, 2009). Stars more massive than eight solar masses which eventually begin fusing Iron peak elements rapidly collapse as those reactions absorb energy rather than create it (Smartt, 2009).

Core-collapse supernova characteristics have more diversity as well as mechanisms for ending a star than thermonuclear ones (Hillebrandt & Niemeyer, 2000).

1.1.2 Supernova Remnants

During the outburst event of each SN, a lot of mass and energy is released which interacts with the surrounding interstellar medium to produce a long-lived, extended supernova remnant. Thermonuclear SNe (from less massive progenitors in binary systems) completely destroy themselves in the explosion and leave behind an expanding SNR.

Supernova remnants are important because they are an energy source for heating and enriching the Interstellar Medium (ISM) and are also thought to be the source of cosmic ray acceleration (Baade & Zwicky, 1934; Ackermann et al., 2013). Additionally, SNR studies help in estimating the mass of the material ejected and provide constraints on the SN progenitor from the abundances in the ejecta (Stephenson & Green, 2002). As of May 2014, 294 Galactic SNRs had been detected and recorded (Green, 2014).

1.1.3 Historical Galactic Supernovae and Their Remnants

Before the era modern astronomical instrumentation, there were few records about historical Galactic SNe. Those records mostly came from Asian regions such as China, Korea, Japan and some Islamic countries (Stephenson & Green, 2002); however, some of the available records are very terse. Hence, there is uncertainty regarding the SNR due to the uncertainty in the original observations. Thus, it is not possible to determine their SN types through these historical records (Green, 2002).

The estimation of the Galactic SN rate is about one SN every 40 ± 10 years; however, most of them will not be seen optically due to dust obscuration (Tammann, Loeffler, & Schroeder, 1994). Most CCSNe happen within a few hundred parsecs of the mid-plane, where recent star formation occurs (Stephenson & Green, 2002).

Green (2002) listed nine SNe as historical, with five of them having occurred in the last millennium. He did not consider the progenitor SN of the Cas A remnant represented in Table 1.1 since the outburst was not plausibly observed in any known historical documents (Stephenson & Green, 2002). Table 1.1 shows a summary of these five pre-telescopic historical SNe and their remnants with the reported duration of peak brightening and the apparent magnitude at the time of discovery. Each historical SN is named according to the year of its discovery. The reported V_{max} values (maximum visible magnitude) in Table 1.1 are very rough estimates that Green (2002) inferred from the apparent magnitudes of known stars and planets that the SN was compared

Table 1.1: Summary of Historical Galactic SNe and their Remnants.

Year	Duration	Magnitude (V_{max})	SNR
1604	12 months	-2.5	Kepler
1572	6 months	-4.0	Tycho
1181	6 months	-1.0	3C58
1054	22 months	-4.0	Crab Nebula
1006	several years	-9.0	G327.6+14.5

Adapted from Green, 2002.

to at its peak. Among the detected SNe in the last millennium, the most recent naked-eye historical record belongs to the Kepler SN which was mentioned in records

from all regions listed above in AD 1604 and remained visible for a full year. Since the famous German astronomer Johannes Kepler observed it and wrote a book on the event in detail, this SN and its remnant have since been named after him (Stephenson & Green, 2002; McDonald, 2012).

2.1.3.1 Cassiopeia A Supernova

The SNR Cassiopeia A, also known as Cas A, 3C461 (the 461st source in the third Cambridge survey), is found at galactic coordinates $l = 111.7°$ and $b = -2.1°$ (Green, 2014). Cas A is estimated to be at a distance of $\sim 11000\ ly$. Before the detection of the 100-year-old SNR G1.9+0.3 (Reynolds et al., 2008), Cas A was the youngest known SNR in the Milky Way. Cas A is one of the brightest sources at radio wavelengths in the sky with a size of 5 arcmin in diameter. Since it was detected as a discrete source in the early days of radio astronomy in the late 1940s (Brown & Hazard, 1953), it was named after the constellation it was in, with A signifiying that it is the brightest object in the constellation (Stephenson & Green, 2002).

Krause et al. (2008) classified Cas A as a Type IIb core-collapse SNe which indicates that the Cas A SN red supergiant progenitor had lost its hydrogen lines before its explosion. Rest et al. (2011) later confirmed the classification of Krause et al. (2008) and detected asymmetries in the outburst. Figure 1.1 shows an image of the Cassiopeia A remnant taken by NASA/ESA Hubble Space Telescope.

Ashworth Jr. (1980) suggested that John Flamsteed in 1680 had observed the Cassiopeia A SN as the last historical Galactic recorded event. Ashworth Jr. identified it in Flamsteed's 1725 catalogue of fixed stars as 3 Cassiopeia (Ashworth Jr, 1980). However, Stephenson and Green (2002) stated that "it is most unlikely that Flamsteed observed the SN which produced Cas A" (page 59). They added that it is very probable

that Flamsteed confused coordinates of two stars in its vicinity, AR Cas and SAO 35386.

Figure 1.1: Image taken with the NASA/ESA Hubble Space Telescope of the SNR known as Cassiopeia A (Cas A). Bands used: R, I and z in 625, 775 and 850 nm, respectively with the Hubble Space Telescope ACS. Credit: (NASA, ESA & the Hubble Heritage STScI/AURA-ESA/Hubble Collaboration, n.d.).

The SNR expansion rate implies an origin of 1681 ± 19 AD (Fesen et al., 2006). However, it is curious that Cas A SN event was not recorded in any historical documents, since from the observations it is thought that Cas A is roughly expected to have occurred in the beginning of the telescope era between the years 1662 and 1700 (Fesen et al., 2006).

2.1.3.2 Tycho Supernova

The Tycho SN, also known as SN1572 and 3C10 (the 10th source in the third Cambridge survey), is found at galactic coordinates $l = 120.1°$ and $b = +1.4°$ has an angular diameter of 8 arcmin (Green, 2014).

It was widely recorded and consequently its lightcurve is reasonably well determined. Since astronomers compared its brightness with Venus ($V_{mag} = -4$), it was one of the brightest observed SNe (Green, 2002; Stephenson & Green, 2002). Because Tycho Brahe was the European astronomer who observed and recorded this event in detail, it is named after him.

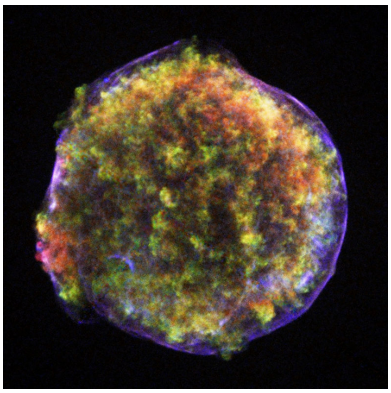

Figure 1.2: Tycho SNR. Chandra's image of the supernova remnant shows an expanding bubble of multimillion-degree debris (green and red) inside a more rapidly moving shell of extremely high-energy electrons (filamentary blue). Color code : Red 0.95-1.26 keV, Green 1.63-2.26 keV, Blue 4.1-6.1 keV. Credit: (NASA/CXC/Rutgers/J.Warren & J.Hughes et al., 2005).

R. Hanbury Brown and C. Hazard (1952) first detected the Tycho remnant at radio wavelengths. Later, Krause et al. (2008) classified the SN as a thermonuclear type after obtaining spectroscopy of a LE at optical wavelengths. The precise distance to the Tycho SNR is uncertain. Some recent studies suggest a value between 2.5 and 3 kpc based on a non-linear rotational curve model (Tian & Leahy, 2011) while others suggest a value between 2.3 ± 0.5 kpc based on optical proper motion and shock velocity (Chevalier, Kirshner, & Raymond, 1980; Albinson, Tuffs, Swinbank, & Gull, 1986; Strom, 1988; Lee, Koo, & Tatematsu, 2004). Figure 1.2 shows an image of the Tycho remnant.

1.2 Light Echoes

When an astronomical transient event such as a nova, supernova, and eruptive variables occurs there are two ways for an observer to detect the light of the event: (a) the event light comes directly to the observer in the line of sight (*LoS*), or (b) the event light encounters interstellar dust and is scattered off it towards the observer. Only a tiny portion of this scattered light ends up in the LoS of the observer (Rest, Suntzeff, et al., 2005). If this *scattered light* is bright enough, then it can be detected (A. P. S. Crotts, 1988) and it is called a *light echo* (LE).

Zwicky (1940) was the first person who suggested investigating historical Galactic SN LEs to learn more about the outburst. During the previous 120 years, all the LEs were found when astronomers were studying the transient and variable objects in their brightest phase. The first LE was discovered about 1901, around Nova Persei (Ritchey, 1901; Couderc, 1939; A. P. S. Crotts, 1988). Crotts (1988) discovered two optical LEs from the extragalactic SN, SN 1987A, for the first time by using coronagraphy. Additional SN LE studies include SN 1987A in the LMC (A. Crotts, 1988; Suntzeff, Heathcote, Weller, Caldwell, & Huchra, 1988), SN 1991T in NGC 4527 (Schmidt et al., 1994; Sparks et al., 1999), SN 1998bu in M96 (Cappellaro et al., 2001), SN 1993J in M81 (Sugerman & Crotts, 2002; Liu, Bregman, & Seitzer, 2003). The first LEs of ancient SNe (i.e., SNe that were unobserved or unrecorded before the era of modern astronomy) were serendipitously discovered in the Large Magellanic Cloud (LMC) when Rest et al. (2005) used difference-imaging[1] during the SuperMACHO Project (Super MAssive Compact Halo Object) (Rest, Stubbs, et al., 2005). The three discovered LE complexes are associated with 0519-69.0, 0509-67.5, and 0509-68.7

[1] Difference-imaging technique will be explained in the Section 1.4

(N103B) SNRs. The discovering of LEs from ancient SNe in the LMC motivated Rest et al. to search historical Galactic SNe fields for LEs (Rest et al., 2007, 2008).

Discovering historical SNe LEs and utilising new and modern instrumentation such as CCDs enabled astronomers to obtain the spectra of these events even centuries later (Welch, 2014; Rest et al., 2015). Astronomers have the rare opportunity to simultaneously study the remnants and the outburst. Additionally, investigating the outburst from different angles allows the asymmetry of the event to be estimated (Rest, Foley, et al., 2011; Rest, Sinnott, & Welch, 2012; Sinnott, Welch, Rest, Sutherland, & Bergmann, 2013).

1.2.1 LE Geometry and Formalism

Couderc (1939) established LE geometry for the first time. Here, we summarize the geometry and formalism of Couderc (1939) and Tylenda (2004).

The nature of LEs is such that the geometry that defines them is an ellipse (ellipsoid in three dimensions) (see Figure 1.3).

The source event is shown as S and Earth as E located at the ellipse foci. The distance between the source and Earth is D. The projected distance is ρ ($= \sqrt{x^2 + y^2}$) while z is the distance of the scattered dust from the source on the line of sight (LoS); hereafter, it is called *echo depth*. Dust location is labelled F, and r ($= \sqrt{x^2 + y^2 + z^2}$) is the distance between it and the source while the dust is at distance l ($= \sqrt{x^2 + y^2 + (D - z)^2}$) from Earth. θ and γ are scattered and separation angles, respectively.

It is known that on the ellipse, the distance travelled from one focus to another, via some point such as F, is the same regardless of the point selected and it is equal to the semi-major axis of the ellipse multiplied by 2. Light takes a longer path through

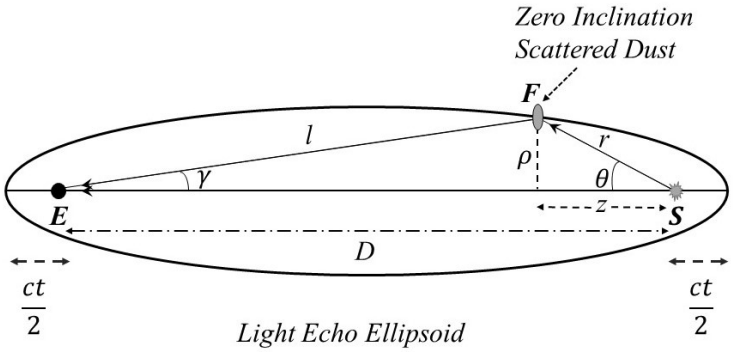

Figure 1.3: Schematically illustrates the geometry of the light echo (LE) ellipsoid. Source and Earth are located in the ellipsoid Foci.

$\overline{SF}+\overline{FE}$ than $\overline{SE}$, so light arrives at E with a time delay (Δt) relative to the observer's LoS as shown in Figure 1.3. So:

$$D + ct = r + l \tag{1.1}$$

where c is light speed. The LE most distant from Cas A in this study is at $\sim 613.5\ pc$ in front of its SNR. The ratio of that distance to D is ~ 0.18. Also, the farthest LE to the Tycho SNR utilized in this study is located 174 pc from its source and its distance ratio is ~ 0.08. So, in practice, $z \ll D$ and we can use the approximation $l \simeq D - z$. Equation 1.1 then becomes

$$ct = r - z \tag{1.2}$$

or equivalently

$$\rho^2 = (ct)^2 + 2ctz. \tag{1.3}$$

This is the equation of a *paraboloid* symmetric around the ellipse major axis (here, LoS) and source event located in the paraboloid focus. Equation 1.3 can be rewritten:

$$z = \frac{\rho^2}{2ct} - \frac{ct}{2} \tag{1.4}$$

which is known as the *light echo equation*. In this equation, ρ is $(D - z)tan\gamma$.

Knowing the angular separation γ and the time since the outburst, the relative distance between the echo and its source ($\frac{z}{D-z}$) can be determined. If the distance between the source and Earth is known, then the echo depth (z) will also be found. Hence, the location of the LE from the source (in front of ($+z$) or behind ($-z$)) can be determined.

1.2.2 Apparent Proper Motion

Light echo equation is the parabola, as discussed in Section 1.2.1. So, as time delay (Δt) increasing, the parabola (as a function of it) is also expands on the sky. Thus, an apparent motion of the LEs can be seen. It is called the *apparent proper motion* (APM) of the LE on the sky. As equation 1.4 shows the LE location on the parabola depends on the ρ and z. Hence, LEs in different locations of the parabola will have different apparent motions. In this section, it is described that the LE APM is also dependent on the inclination of the scattered dust.

Couderc (1939) suggested two cases for scattering geometries: thin filaments and a

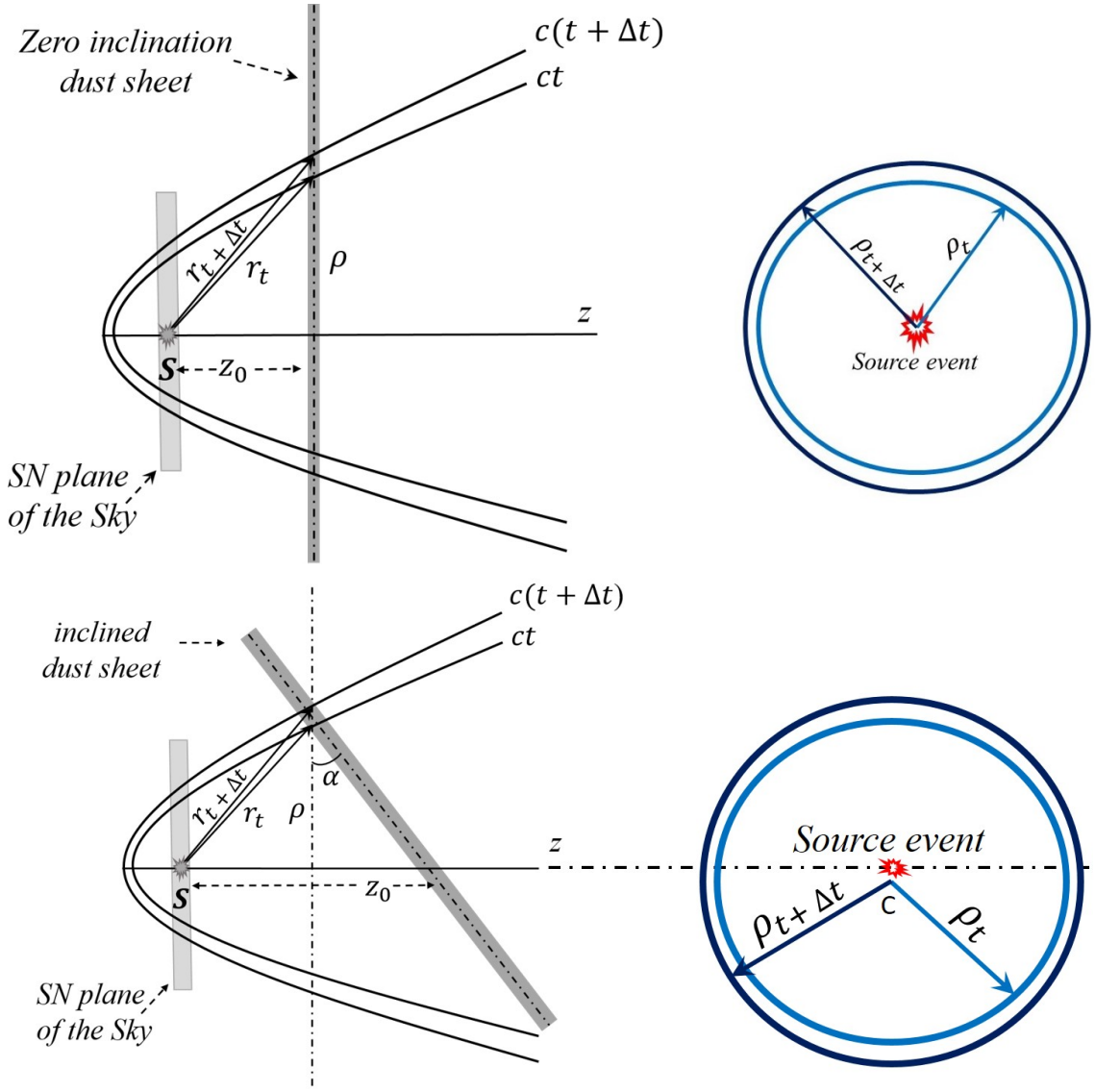

Figure 1.4: Top: Schematically demonstrating the apparent motion of the LE with zero inclination in interval Δt. Bottom: The same figure as the top panel except the dust sheet has an inclination equalling α. In both panels, the source is at the focus of the parabola. The dash-dotted line shows the projected distance perpendicular to the line of sight, ρ. The gray rectangle illustrates the dust sheet. Additionally, concentric circles schematically show that what an observer sees in the sky is the projected LEs on the plane perpendicular to the line of sight.

sphere shapes. Sugerman et al. (2012) found that for multiband observations, thin filaments are the best explanations for LEs. Figure 1.4 demonstrates the expansion

of the LE ellipsoid on the sky and the intersection of the dust filament with this LE ellipsoid expansion. In both panels of Figure 1.4, the inner parabola indicates the time delay t and the outer one shows the time delay $t + \Delta t$ such that the additional travelled distances are ct and $c(t + \Delta t)$ where c is the speed of light.

The dust sheet, dark-gray thin rectangle in the panels, intersects the LoS, or the z-axis, where the angle α is the inclination angle. It is considered an angle between the normal line (ρ-axis) to the LoS and the dust filament in both panels and also defines the angle from the positive ρ-axis toward the negative z-axis. The top panel of Figure 1.4 demonstrates the inclination $\alpha = 0$ and all the formalism mentioned in Section 1.2.1 can be used for this case. The bottom panel illustrates the non-zero inclined dust sheet. Concentric circles in both the top and bottom panels schematically illustrate that circular rings are observed on the sky in an observer's LoS regardless of the dust sheet's inclination, but the bottom case is not centred on the source event.

Neglecting the inclination can lead to a significant bias in LE APM estimation. Considering Couderc (1939), Tylenda (2004), and Rest et al. (2012), the LE equation (Equation 1.4) is expanded to describe the case of an inclined dust sheet. Here, if $z = z_0 - a\rho$ where $a = tan\alpha$, then

$$\rho = -act \pm \sqrt{(1 + a^2)(ct)^2 + 2ctz_0} \tag{1.5}$$

where $\sqrt{(1 + a^2)(ct)^2 + 2ctz_0}$ is the radius of the LE rings appearing on the plain of the sky and $-act$ is the offset of the LE rings' center. Taking the time derivative of Equation 1.5 gives the apparent proper motion of the LE ring on the sky:

$$\dot{\rho} = c \times \{-a \pm \frac{(1 + a^2)(ct) + z_0}{\sqrt{(1 + a^2)(ct)^2 + 2ctz_0}}\} \tag{1.6}$$

where considering $-45^\circ \leq \alpha < 0^\circ$ leads to $\dot{\rho} \to \infty$ which is apparently superluminal.

Similarly, if the dust sheet has inclination α equal to $0°, 45°$, and $90°$, then $\dot{\rho}$ will be apparently equal to $1.0c, 0.5c$, and $0.0c$, respectively. Note should be taken that $\dot{\rho}$ is the apparent proper motion of the LE projected on the plane of the sky, perpendicular to the LoS. The measurements made in this thesis of APM are the rates of the angular separations of LEs with time:

$$\dot{\gamma} = (\frac{\cos^2\gamma}{D-z}) \times (c \times \{-a \pm \frac{(1+a^2)(ct)+z_0}{\sqrt{(1+a^2)(ct)^2+2ctz_0}}\}). \tag{1.7}$$

Most of the LE APMs discussed in this thesis are $\simeq 30\ ''yr^{-1}$.

In the next section, some background research on the LE APM estimation will be discussed.

1.2.3 Background Research on the LE APM Estimation

In this section the previous method used to estimate APM by Rest, Suntzeff, et al., 2005, Rest et al. (2008), and Rest et al. (2012) is described.

Recall that Rest, Stubbs, et al., 2005 serendipitously discovered the first ancient extragalactic SNe LEs when they were working on the the SuperMACHO Project (Rest, Suntzeff, et al., 2005). The left panel of Figure 1.5 is an image displaying individual light echo proper motion vectors (Rest, Suntzeff, et al., 2005), and the right panel presents the LE APM vectors and the position of several-centuries-old SNe in the Milky Way (MW) (Rest et al., 2008). To measure the LE APM vectors, Rest et al. used the following method. First, they divided the LE images into small arclets, then drew a line tangent to the arclet on the LEs. Next, they visually estimated the arclet motion directions, which are demonstrated by yellow vectors (perpendicular to the

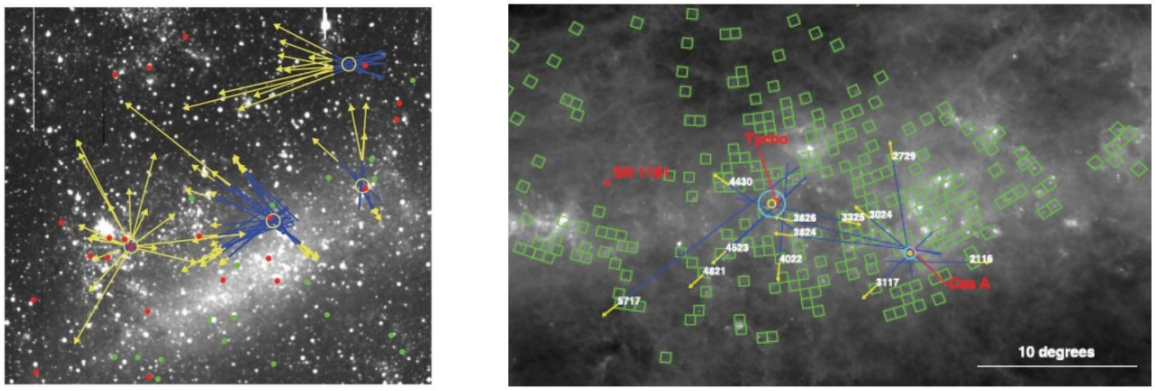

Figure 1.5: The apparent proper motion vectors are shown by the yellow vectors and continued reversely with blue lines towards the SNRs . The left panel is adapted from Rest, Suntzeff, et al., 2005 and the right from Rest et al. (2008). The source on the left of the left panel is SN1987A.

related arclet) in the panels of Figure 1.5. The researchers then estimated the position of the SNR at the crossing point of the vectors, by calculating the crossings of all pairs of vectors and excluding any echo pair with a separation of less than $10''$. They mentioned that the unknown inclinations of the dust filaments leads to a possible bias of the APM and measured the SNR positions within the standard deviation of the points of origin.

1.3 Review of Observation Materials & Reduction Technique

This section reviews the instrumentation used including the selected observatory, its imager, and its other facilities. Finally, it describes the reduction technique steps which were taken by Armin Rest and his group to prepare difference-images [2] by using

[2] The concept of difference-images is introduced later in Section 1.4.

the Pan-STARRS (Panoramic Survey Telescope and Rapid Response System) pipeline before the LE images were selected by Professor Doug Welch for this study.

1.3.1 Instrumentation

All of the astronomical images were taken at the Kitt Peak National Observatory (KPNO) with the Mayall 4-meter telescope during several observational seasons. Armin Rest and his colleagues performed these observations from 2006 to 2011 as described in their proposal "Echoes of Historical Supernovae in the Milky Way Galaxy"(Rest, Sinnott, et al., 2011; McDonald, 2012; NOAO, 2014). The goal of their proposals was surveying for light echoes in the fields near Cas A, Tycho, SN1181 and SN 1054. As a result of this observing program, they found LEs for Cas A and Tycho but were unsuccessful finding LE systems for SN1181 and SN1054. Table 1.2 provides a summary of the Rest et al. observing runs (NOAO, 2014).

Table 1.2: Summary [(1)] of A. Rest and his group's LE program at the KPNO.

Obs. Yr. [(2)]	PI# [(3)]	PI [(4)]	Details
2006	0301	N. B. Suntzeff	4 nights, Oct. 20-23
2007	0332	A. Rest	4 nights, Oct. 12-15
2009	0493	A. Rest	4 nights, Sept. 14-17
2011	0130	A. Rest	2 nights, Step. 22-23

(1): Rest et al. utilized the 4-meter telescope and Mosaic-1.1 imager for their observations at KPNO. (2): Year of observation. (3): Proposal number. (4): Principal Investigator. (NOAO, 2014).

The two primary motivations for using the 4-m telescope KPNO were: (a) the northern hemisphere location, which makes it appropriate for searching for LEs of all the historical Galactic supernovae in the northern hemisphere and (b) it is equipped with

a wide field-of-view (FOV) CCD camera ($36' \times 36'$), the Mosaic-1.1 imager (MOSA) (Schweiker, Howell, & Sawyer, 2011) whose format is 8192×8192 pixels. Thus, Mosaic-1.1 covers approximately 0.25 square degrees of sky. This imager contains eight CCDs, each of which is read out using two amplifiers (Figure 1.6) (Schweiker et al., 2011). The final image data are written in 16 Header/Data Units (HDU) called extensions (Pence, 2014), one for each CCD amplifier (Schweiker et al., 2011). Mosaic-1.1 produces Flexible Image Transport System (FITS) images (Wells, Greisen, & Harten, 1981), which are the astronomical standard data format for transporting, analyzing, and archiving scientific data files.

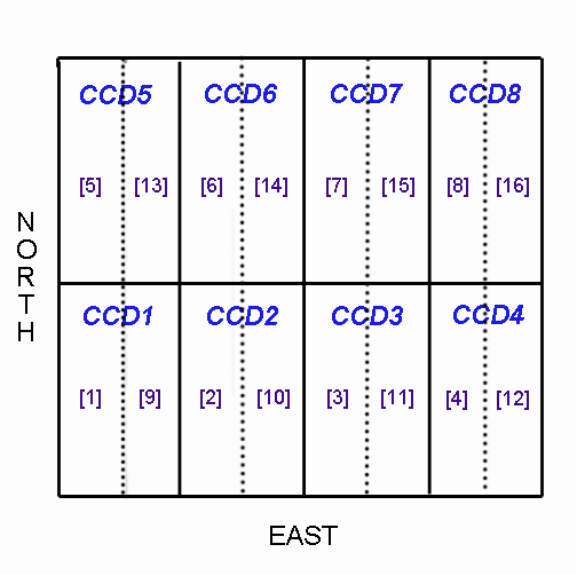

Figure 1.6: The display orientation of the 16 sections of the Mosaic-1.1 imager on the Mayall 4-m. The 8 CCDs are divided up into a total of 16 amplifiers that are labelled in the figure as the numbers in square brackets (Schweiker et al., 2011).

Rest et al. used the broadband VR Bernstein (k1040) and VR k1039 custom filters. The VR Bernstein filter had a central wavelength of 5944.95 $\mathring{A}$, a FWHM of 2119.56 $\mathring{A}$ and a peak transmission of 95.40%. This filter was damaged in June 2011 and was consequently retired. Since then, the VR k1039 has been used at KPNO. It

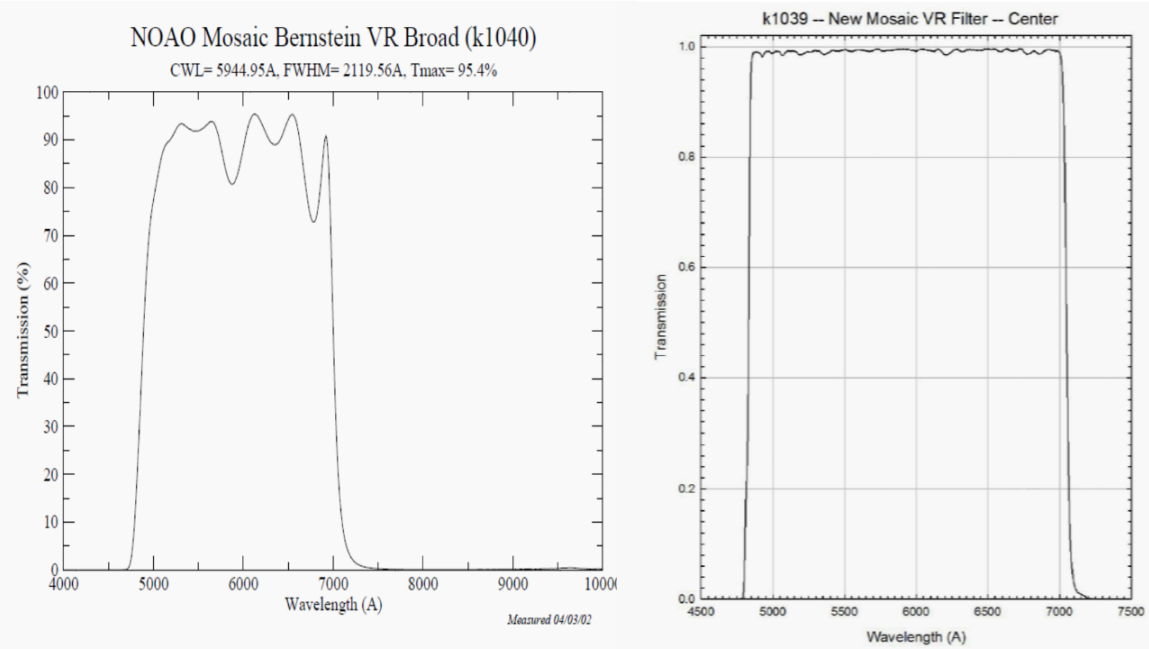

Figure 1.7: Left: Retired Mosaic Bernstein VR broadband (k1040) was measured on April 3, 2002 . Right: New Mosaic VR filter (k1039) was measured on Mach 31, 2014 (Schweiker, 2015).

has a central wavelength of 5940 $\mathring{A}$, a FWHM of 2216 $\mathring{A}$, and a peak transmission of 99.46%. Figure 1.7 shows the transmission curves for these filters in parallel light. Choosing such a broad bandpass allowed them to record more photons per unit time than traditional filters. Table 1.3 shows some characteristics of the Mosaic-1.1 imager (Schweiker et al., 2011).

1.3.2 Pre-Processing Steps

The ten difference-images used in this study were prepared by Armin Rest and his group and processed by the Pan-STARRS pipeline. Professor Doug Welch selected the 10 mentioned difference-images for this study. In the following, some general

Table 1.3: Summary of Mosaic-1.1 characteristics [1]

Arrays	Eight 2048 × 4096 e2v CCDs (4 × 2), (see Figure 1.6)
Image size	8192 × 8192 pixels
Pixel size	15 μm (0.26″/pixel at the 4-m telescope)
Filters [2]	VR Bernstein k1040 (retired in June 2011 [3])
	VR k1039 (It is now available as a replacement)

(1): (Schweiker et al., 2011). (2): A. Rest et al. used these filters in their program (McDonald, 2012). (3): (Schweiker, 2015).

reductions are explained that might be performed by the Pan-STARRS pipeline.

Image Pre-Processing

The first steps in preparing CCD data to be analysed are to remove the bias and flat-field pattern in the raw images. Data should characterize the astronomical source under investigation and not the detector, telescope, terrestrial atmosphere, scattered light by the optics through the telescope, or any other perturbing element. These very first steps in reducing array data must be carried out on all CCD data.

Bias Bias is a voltage applied to the detector to ensure a positive readout value even in the absence of photons. Bias frames are taken with a zero-second exposure and with no light incident on the detector. In this case, the positive output from a zero-time exposure is called the *bias level*, or the *zero level*, and will be present in every frame as a quantity added to the output (Chromey, 2010).

Flat-Field Response An important processing step is correcting for the pixel-

to-pixel variation in sensitivity of the CCD camera. Ideally, an image of a perfectly uniform or "flat" target is taken with the complete observing system including the detector, telescope, and any elements like filters that influence the focal-plane image. *Dome flats*, *dark-sky* (or night sky) *flats* (or illumination corrections) and *twilight flats* are examples of this kind of calibrating data.

Images from an illuminated nearby object like a white screen as a flat-field target inside the observatory dome are called dome flats. The advantage of this calibration source is that the astronomer is enable to control the spectrum and intensity of the illumination.

Blank field flats are another type of flat-field correction since the spectrum of the dark (i.e. moonless) night sky is perfectly uniform at zenith and the regions near to it.

Twilight is not uniform in different directions; the sky is brighter especially in the direction of the sun near sunset or sunrise. A disadvantage of this technique is the short interval over which images can be collected. Brightness and illumination are almost uniform; however, light levels vary rapidly with time (Chromey, 2010).

Dark response A dark response depends on the camera temperature and exposure time. Hence, the detector is exposed for time t with shutter closed. If there are non-linear effects, it is necessary to obtain dark frames with exposures similar to the those of the science images (Chromey, 2010), since changing the mentioned parameters between a dark frame and light frame can cause a mismatch between acquired frames.

Artefact Usually, artefacts are related to pixel signals that do not have a natural source, such as a *dark response*. Also, the term *artefact* is used for explaining any unexpected gained signal by CCD pixels such as cosmic rays.

Crosstalk Crosstalk is the low-level electronic current pickup between the amplifiers of a CCD, since signals are transferred by amplifiers simultaneously during the CCD readout (see Figure 1.8) (Schweiker et al., 2011).

Trailing Ghosts These are specific to the Mosaic camera. Bright stars that saturate the detector sometimes produce ghost images that trail the stars in the readout direction (see Figure 1.8); this means that along the row away from the output amplifier (Schweiker et al., 2011).

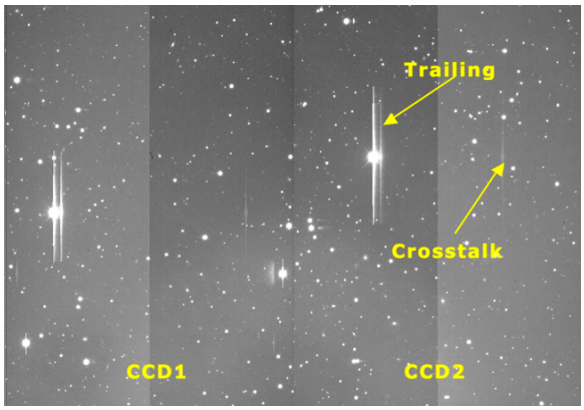

Figure 1.8: Image of (full-well) saturated stars showing the effects of crosstalk between CCD outputs and the "trailing ghost" anomaly (Schweiker et al., 2011).

Saturation, Blooming and Diffraction Spikes In an ideal detector, the output signal is directly proportional to the input illumination. However, if a CCD pixel's potential well gets filled and cannot store any more charge carriers, then the electrons spill into the neighbouring pixels; this peak value in the reduced images is called the *saturation* limit.

Blooming is the spilling of charge along a column or a row of the CCD. It happens as a result of saturation occurring before the CCD receives a readout. CCD rows are less affected by blooming due to the way that CCDs are fabricated.

Diffraction spikes are radial lines radiating from bright stars in reflecting telescope images due to the effects of the support beams of the prime focus camera (see Figure 1.9) (Chromey, 2010).

Astrometric Calibration This is the mathematical transformation between a CCD's pixels positions and celestial coordinates on the sky. Applying an astrometric

Figure 1.9: Blooming on a CCD image: the saturated vertical columns are the bloom. The other linear spikes on the bright star image result from diffraction by the vanes supporting the telescope's secondary mirror (Chromey, 2010).

calibration, we can create a World Coordinate System (WCS) for astronomical images that is restored in the image header.

Ghost Pupil This is the faint image of the telescope pupil that forms on the CCD (Schweiker et al., 2011) (see Figure 1.10). Ghost pupils are produced by KPNO 4-meter prime-focus correctors from light that reflects off filters, then off the back surface of the detector, and then returns through the filters to the science detectors (Jannuzi, Claver, & Valdes, 2003). There is no way to avoid recording these.

Next Steps in the Image Processing

Image Summing When there is more than one image from one epoch, it is beneficial to sum the images. Before summing, the images must be aligned. This happens after the pre-processing stage.

To align a set of images from one epoch, one image is chosen as a reference image. Then, other images are resampled to the same geometry as the reference image; i.e., removing the effects of optical distortions due to the telescope pointing differences. A

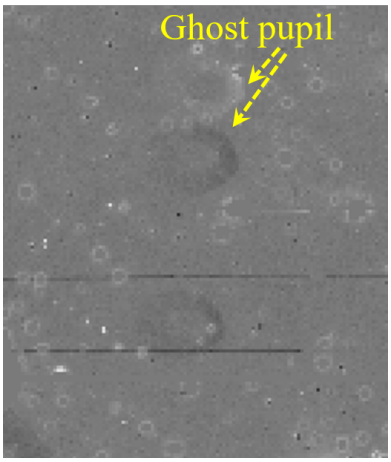

Figure 1.10: Some ghost pupil effects, which are like bright and dark rings are seen in the top center of the difference-image. This image appeared in one of our studied difference-images.

software package called SWarp (Bertin et al., 2002) is used to achieve this prior to summing the transformed images.

Cleaning Images Inevitably, the images have some defects due to bad detector pixels, unwanted radiation events like cosmic rays, saturations, etc. To clean these defects, a "*mask*" is used, which sets the value of the defective pixels to zero in the difference-image.

Point-spread Function For a point source detected by a particular telescope, the run of intensity with angular or radial distances from the image center is called the point-spread function (PSF). When PSFs of two images are matched, the images are ready for subtraction or difference-imaging. Generally, since images are taken under different conditions, such as zenith angle, exposure times, or atmospheric seeing, each image will have a different PSF. Therefore, an important task is matching the PSF of different images by using a *convolution kernel*. Image convolution is an elementary type of digital filtration. The *kernel* of the convolution is a matrix to filter the PSF out of the images and transform the original image to a new image. Therefore, a pixel

in the output image is a weighted sum of the input image's pixels with a kernel of a certain size. Alard and Lupton (1998) used a constant kernel, but since the PSF varies spatially, especially in larger images, Alard (2000) suggested that the kernel must be modelled as a spatially varying function.

1.4 Difference-imaging

Difference-imaging is a method used to find objects that vary in brightness and/or position. Difference-imaging produces a digitally-subtracted image of the same field of the sky taken at different epochs. To achieve useful difference-images, it is necessary to remove or reduce the defects in images.

Figure 1.11 schematically represents difference-imaging. Panel *a*-1 presents the telescope view of the selected area of the sky in the first epoch of observation. Panel *a*-2 shows the telescope view of the same area of the sky after a while as a second epoch of the observation. Background stars are shown with the circles and ellipses in both panels *a*-1 and *a*-2. In panel *a*-1, the illuminated dust filament (top left of the panel) and some stars are appeared while in the panel *a*-2, the background stars are constant and the second illuminated dust filament is shown in the bottom right of the panel. Since only the filaments differ in position, after differencing panel *a*-2 from the panel *a*-1, the result will be illustrated as panel *b* where the first illuminated dust is darker than the difference-image field and shows a negative deviation. The second illuminated dust filament is brighter than the field of the difference-image and shows a positive deviation. In other words, first and second filaments have negative and positive pixel values, respectively. Since LEs are extended moving astronomical features of varying size and shape, difference-imaging can be used to search for them.

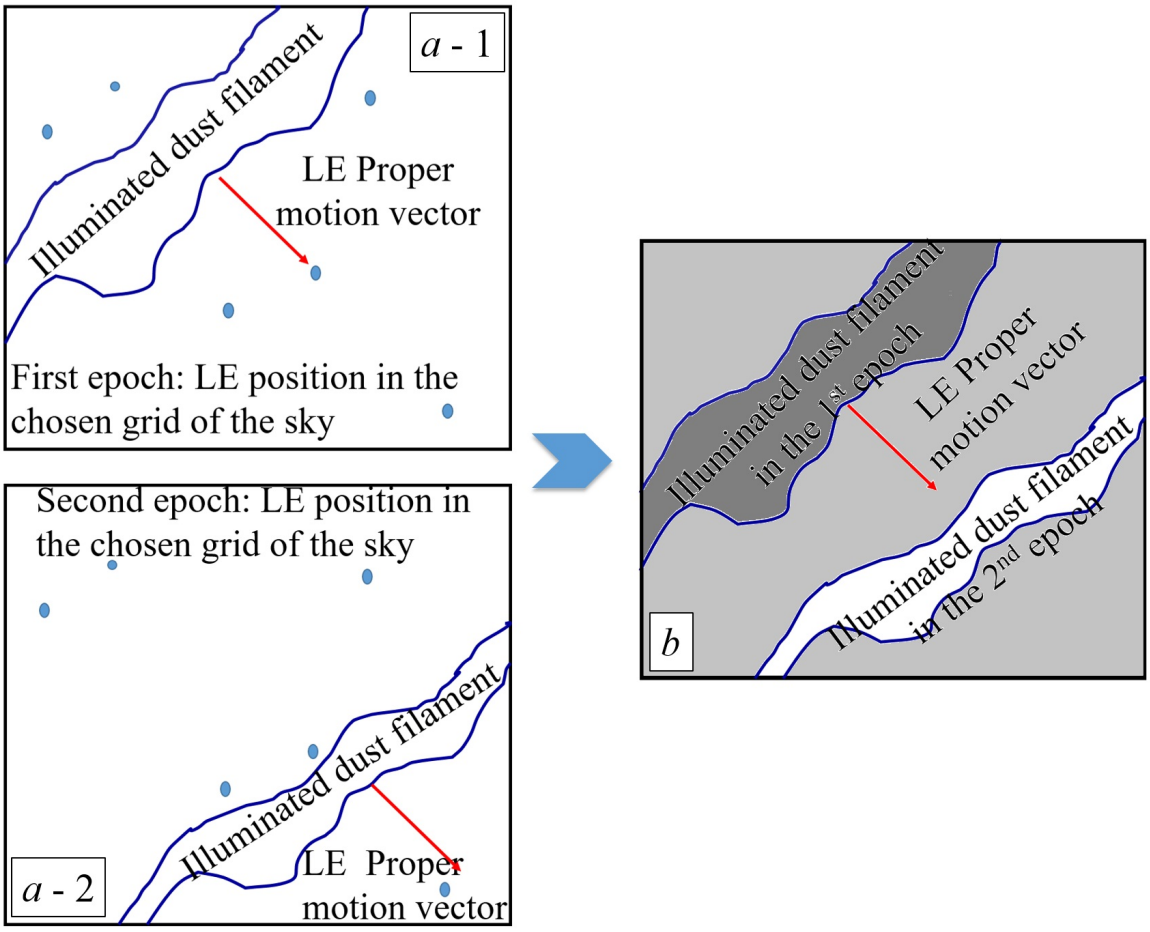

Figure 1.11: *a*-1. Schematic illustrates the detected LE in the chosen grid of the sky for the first time. *a*-2. Second detected LE in the same chosen grid of the sky. In both a-1 and a-2 images, the telescope view covers exactly the same area of the sky. Circle and oval shapes represent bright stars in the sky field. *b*. Schematic difference-image of the *a*-1 and *a*-2 images. Dark gray indicates the LE feature from the first epoch of the observation and white shows the LE feature related to the second epoch.

In the next chapter, difference-images will be used to perform a new mathematical and computational method to estimate the LE apparent proper motion (APM) and its uncertainty by introducing and utilizing cross-correlation and full width at half maximum methods.

Chapter 2

Methodology

This chapter describes in detail the method taken to perform the cross-correlation (CC) technique and to consequently find the apparent proper motion (APM) of the light echoes LEs. Then, the preparation method for difference-images for cross-correlation step is explained. After that, LE apparent proper motion (APM) vector estimation is described. Finally, this chapter describes how to find the uncertainty of the APM.

As discussed in the previous chapter, LEs are the scattered light of transient events such as supernovae (SNe). They are reflected off filaments of interstellar dust. The location of the dust filaments in the interstellar medium does not changeover time but the location of the illumination does.

Figure 1.11*b* schematically illustrates a difference-image with LE features from the first and second epochs of the observation indicated by dark gray and white, respectively.

After explaining the cross-correlation method and the usage of this computational method in two dimensions, Section 3 will describe how two sub-difference-images are prepared to perform the CC process. Figure 2.1 demonstrates how two sub-difference-images are prepared as positive and negative portions of the difference-image of Figure

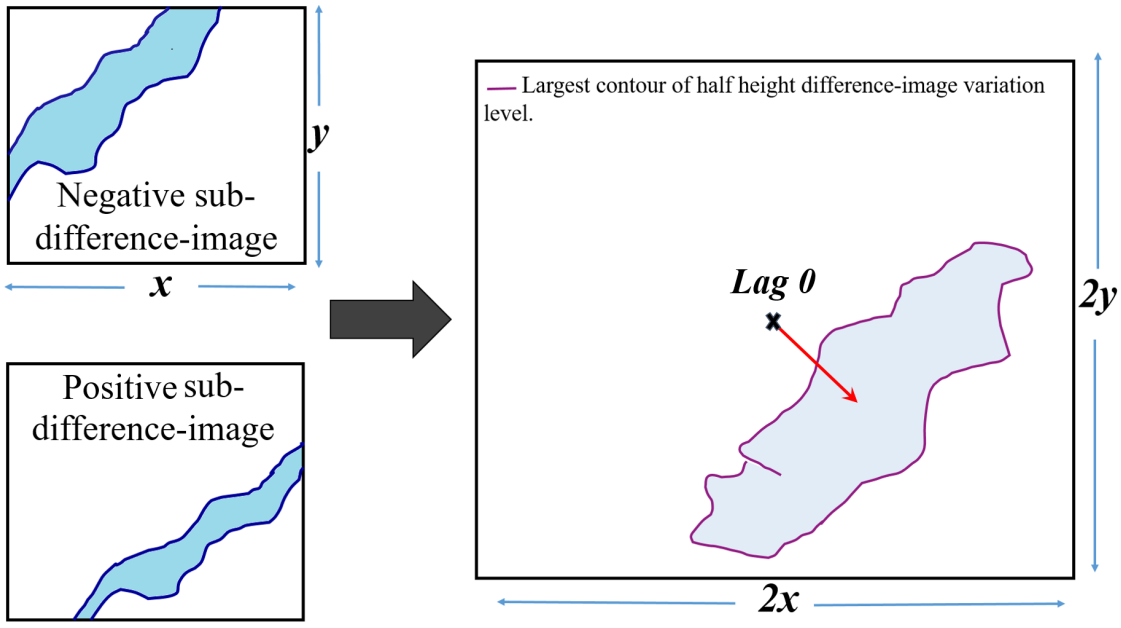

Figure 2.1: Left top and bottom: Schematics of idealistic negative and positive difference-images, respectively. Right: Schematic LE cross-correlation image. The length and width of the CC image are 2 times the dimensions of the difference-image.

1.11*b*. These two sub-difference-images are ideal. In section 2.4, it will be explained that it is, in practice, unlikely to have only one of the LE features in each of the positive and negative sub-difference-images. After that, cross correlating the two sub-difference images will produce an image called a *cross-correlation image* (right panel in Figure 2.1). Cross-correlation image size and Lag 0 will be explained in Sections 2.3 and 2.5, respectively.

There are some limitations in estimating the proper motion of the LEs. If there are any LEs in the chosen field of view, only part of the dust filament may appear in the image. Furthermore, based on the image boundaries, we do not know how far the filament extends beyond the image boundary.

Figure 1.11a-1 and 1.11a-2 schematically show the limitation of covering the illuminated dust in the same grid of the telescope view but at two different epochs; i.e., the telescope view covers exactly the same area of the sky in both epochs.

The opportunity to estimate the uncertainty in the proper motion is the most important advantage of using this computational method, which is described in Section 2.3. Since this thesis aims to properly account for the limitations in the LE proper motion estimations, finding the standard deviation of the LE proper motion value by *full width at half maximum* (FWHM) method is an appropriate approach. The FWHM method is fully described in Section 2.7. The schematic on the left of Figure 2.2 reveals the red vector that gives the estimated APM vector of the LE features. The schematic on the right demonstrates fitting an appropriate tilted ellipse to the half-peak of the cross-correlation's largest contour. This ellipse is then used to obtain the uncertainty of the proper motion which is the final goal of this chapter.

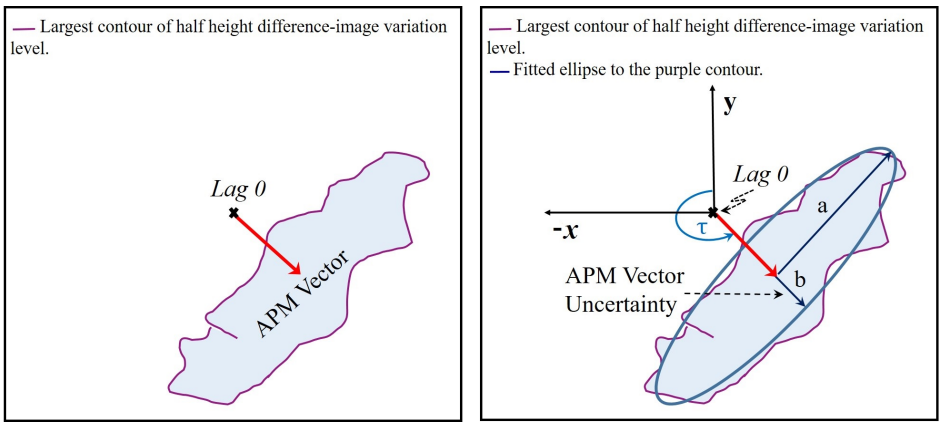

Figure 2.2: Left: Schematic LE cross-correlation image. Right: An ellipse is fitted to the half-height largest contour on the LE cross-correlation image.

Therefore, after preparing the positive and negative sub-difference-images from the difference-image, 2-D CC can be performed in order to obtain an estimate of the LE proper motion. In this chapter, first the ten selected difference-images and their

characteristics are introduced. Then the 2-D CC is described, followed by a discussion of the specific technique that is used to obtain the estimated APM vector and its uncertainty. All the codes were developed in the MATLAB environment.

2.1 Difference-images Used in the Current Study

Armin Rest and his group used the Pan-STARRS pipeline to prepare difference-images, and Professor Doug Welch selected ten difference-images from them. These difference-images were used to study LE APM of SNRs Cas A and Tycho. Table 2.1 provides the summary of these difference-images. There is a special case in Table 2.1, the first epoch of the LE#1 difference-image was taken by another research group whose Principal Investigator was Rachel Mandelbaum in 2009. The second epoch was taken later by Rest et al. according to their schedule in September 2011, as were the rest of the images as mentioned in the Section 1.3.1 (see Table 1.2).

Columns one and two presents LE names by number and their event source. The equatorial coordinates of the LEs are presented in column 3 and 4 of Table 2.1. The first date of the LE observation appears in the column 5 and the time interval between the first and second epochs is listed in the column 6. The last column shows the amplifier number on which each LE was found. This number indicates which amplifier of the CCD camera the image data was read from (see Section 1.3.1 and Figure 1.6).

2.2 Cross-Correlation

Using the CC, astronomers are able to measure how similar two different observable quantities are at different times (Scargle, 1989), i.e., the CC function indicates how similar the time series observations are as a function of the time delay. Tonry & Davis

(1979) presented an implementation of cross-correlation and demonstrated the theory behind it. Cross-correlation is one of the most important applications of the Fourier transform (FT).

Table 2.1: Difference-images discussed in this thesis

LE number	SNR	RA (hh:mm:ss)	Dec (deg:mm:ss)	1st Epoch	Interval (in years)	Amplifier number
LE#1	Cas A	23:12:16	+59:34:29	23.06.2009	2.250	8
LE#2	Cas A	23:35:07	+55:07:31	13.10.2007	1.928	5
LE#3	Cas A	23:46:39	+57:44:37	12.10.2007	1.931	4
LE#4	Cas A	00:20:55	+61:17:10	12.10.2007	1.931	5
LE#5	Cas A	00:21:01	+61:17:05	12.10.2007	3.948	5
LE#6	Tycho	00:22:32	+62:15:42	12.10.2007	1.931	3
LE#7	Tycho	00:22:09	+62:13:38	12.10.2007	1.931	7
LE#8	Tycho	00:28:19	+60:05:57	12.10.2007	1.931	1
LE#9	Tycho	01:04:44	+59:14:21	22.10.2006	2.901	5
LE#10	Tycho	01:06:02	+59:33:14	20.10.2006	1.150	8

2.2.1 Cross-Correlation as a Fourier Transform Application

Using CC, astronomers can assess how similar two images are to each other. For two images taken at two different epochs, CC takes all the values of the second epoch image and compares them with the values of the first epoch image, pixel by pixel. Where the second epoch image is most similar to the first epoch image, a strong maximum

peak appears, i.e., the highest value of the CC represents the position where the two images are best matched.

Since images are represented by two-dimensional discrete functions, for instance $f(x, y)$ and $g(x, y)$, it is appropriate to introduce the 2-D cross-correlation function, $C(i, j)$, which is generally [1] given by:

$$C(i,j) = \int_{-\infty}^{\infty} f(x,y)g(x+i, y+j)dxdy. \tag{2.1}$$

Equation 2.1 builds a CC map with indices i and j from the product of the two images, $f(x, y)$ and $g(x, y)$, of the same sky field at different times. It means that the first pixel value of the first epoch image multiplied by the first pixel value of the second epoch image and its product is added to the product of the next pixel values of the two images, and so on. The entire sum of these products is the CC or the value of the CC map at that particular position.

The sum of the product effectively assesses the similarity of the two images at two different epochs. The best way to calculate the CC function is to take advantage of the *cross-correlation theorem* which states that the Fourier transform of the CC of two functions is equal to the product of the individual Fourier transforms, where one is the complex conjugate of the other:

$$\mathcal{F}\{f \star g\} = \overline{(\mathcal{F}\{f\})} \; . \; \mathcal{F}\{g\}. \tag{2.2}$$

The CC is represented by the pentagram (i.e., $\star$) symbol, $\mathcal{F}$ denotes the Fourier

[1] Since the cross-correlation function is used between two discrete functions, the correct method is to consider the sign Σ instead of $\int$. The discrete cross-correlation function is shown and discussed in Section 2.3.

transform, and the bar indicates the complex conjugate. Thus, CC will be obtained via:

$$C = \mathcal{F}^{-1}(\overline{(\mathcal{F}\{f\})} \; . \; \mathcal{F}\{g\}). \tag{2.3}$$

In Equation 2.3, $\mathcal{F}^{-1}$ denotes the inverse of the FT.

The Fourier transform is a periodic function (such as $\sin(\theta)$ and $\cos(\theta)$), so obtaining CC by using a discrete FT is also cyclic with a period corresponding to the length of the longest component of the correlation. If this periodicity is not taken into account, the CC will wrap around the ends and possibly "contaminate" the resulting function. Zero-padding (i.e., considering the edge of at least one function equal to zero) the input functions solves this issue (Condon & Ransom, 2010).

2.3 Cross-Correlation in Two Dimensions

Matrices N and P represent the negative and positive sub-difference-images and their lines and columns are pixel coordinates. Both matrices P and N are the same size since they are both produced from a single subtracted image. The 2-D CC of an $M \times N$ matrix P and an $M \times N$ matrix N is given by a matrix C of size 2M–1 by 2N–1 in the MATLAB environment (Pence, 2014):

$$C(li., col.) = \sum_{-m+1}^{m-1} \sum_{-n+1}^{n-1} P(m,n)\overline{N}(m - li. \; , \; n - col.) \tag{2.4}$$

$$where \begin{cases} -(M-1) \; \leq \; li. \; \leq \; (M-1) \\ -(N-1) \; \leq \; col. \; \leq \; (N-1) \end{cases}$$

and the bar over N denotes complex conjugation. "*li.* "and "*col.* "are used as abbreviations for the number of lines and columns of the matrices, respectively. Thus, $C(li., col.)$ is given the CC value in two x- and y-directions.
Changing the column numbers from $(-n+1)$ to $(n-1)$ and lines from $(-m+1)$ to $(m-1)$ lead to finding the maximum values of CC based on *lags*, i.e., the CC function is calculated by moving one image over the other pixel by pixel in the x- and y-directions, respectively. Thus, the length and width of the CC images are two times those of the difference-image.

2.4 Common Characteristics of Difference-Images

The Pan-STARRS pipeline was used by Armin Rest's group to produce the difference-images; however, some additional tasks needed to be performed to fully prepare them for the cross-correlation step. In order to decrease the negative effect of artefacts and enhance the strength of LE features in the cross-correlation process, a region from each difference-image was chosen restricted to the area containing all apparent LE features which hereafter is called the *LE region image*. The following issues are common between the LE region images:

1. **Eliminating the Non-LE Variables, Residual Saturations, and Dead Pixels:**

   During the removal process of adjacent variable objects and residual features, i.e.,saturated and dead pixels, in the LE region image, if the masking process is done inadequately, it can leave residual point-spread-function (PSF) wings in the difference-images and small high-value regions which will also complicate the interpretation of the CC image. To reduce this issue, the masking process was re-done on the LE regions to improve the LE CC values. This means that the value of these variables and non-LE features are manually set to zero by

considering a rectangular area around them in the developed code. In this way, these non-LE variables and features cannot take part in the CC result. So, the more accurate the masking is, the better and narrower is the range for CC uncertainty.

2. **Control the Range of Pixel Values:**

   Dead pixels and residual saturations have high negative and positive pixel values, respectively. Neglecting these defects negatively affects the minimum and maximum pixel values of the LE region difference-image. Thus, the defects will negatively affect the CC process and can lead to a bias in the CC result. Using the packages IRAF and DS9, the approximate range of LE pixel values was found through visual inspection and defined a certain pixel value range according to the LE pixel values. Then, values outside this range are set to zero. Therefore, the effects of incorrect lower and higher artefact values are reduced. If there are any remaining residual saturated or dead pixels in the LE region, there will be some in the range of the LE pixel values. So, the CC result will be improved. Figure 2.3 shows the difference-image of LE#4 before eliminating the non-LE variables, residual saturations, and dead pixels in the left panel and also after eliminating them in the right panel.

3. **Preparing Two Sub-Difference-Images:** After eliminating the non-LE variables, residual saturations, and dead pixels, two sub-difference-images for each LE region image were prepared:

   (a) **Positive and negative images:** Two sub-images were prepared: one positive and one negative. The positive sub-image is built based on the positive pixel values of the LE region difference-image, ignoring the negative pixel values. The negative sub-image is made based on the negative pixel values of the LE region difference-image.

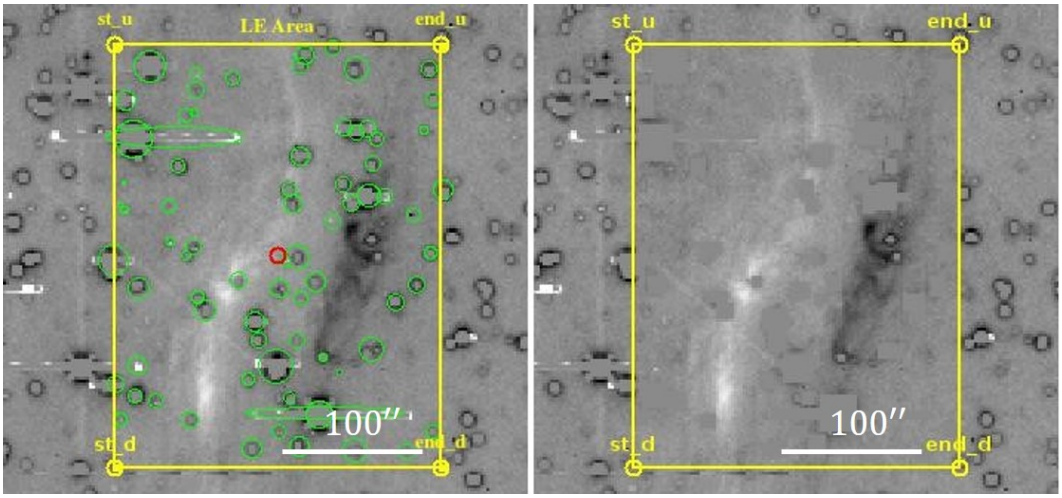

Figure 2.3: Left: The difference-image of LE#4 before eliminating the non-LE variables, residual saturations, and dead pixels. The green circles and ellipses show these defects and the red circle shows the center of the yellow box. The yellow box in the left and right panels indicates the region considered a difference-image. Right: The difference-image of LE#4 after eliminating the defects identified in the image on the left.

(b) **Multiplying the Negative Image by (-1):** All pixel values of the negative sub-image are multiplied by (-1) to make the values positive. Since it is important that during the performing 2-D CC process no negative value exists, this step is critical. Hereafter, whenever the negative image is mentioned, it will refer to the negative sub-difference-image multiplied by (-1).

Figure 2.4 shows both positive and negative sub difference-images of LE#4. The expectation is that in each of the positive and negative sub-difference-images only one of the LE feature epochs should appear. However, all the pixels in the LE difference-image have positive or negative values. Thus, the other LE feature epoch is also visible in the sub-difference-images as can be seen in Figure 2.4 as a pattern of zero value pixels.

In Section 2.5, the *control region image* will be introduced. Then, it will be argued that in order to improve the CC process, running tasks 2 and 3 discussed in this section are necessary.

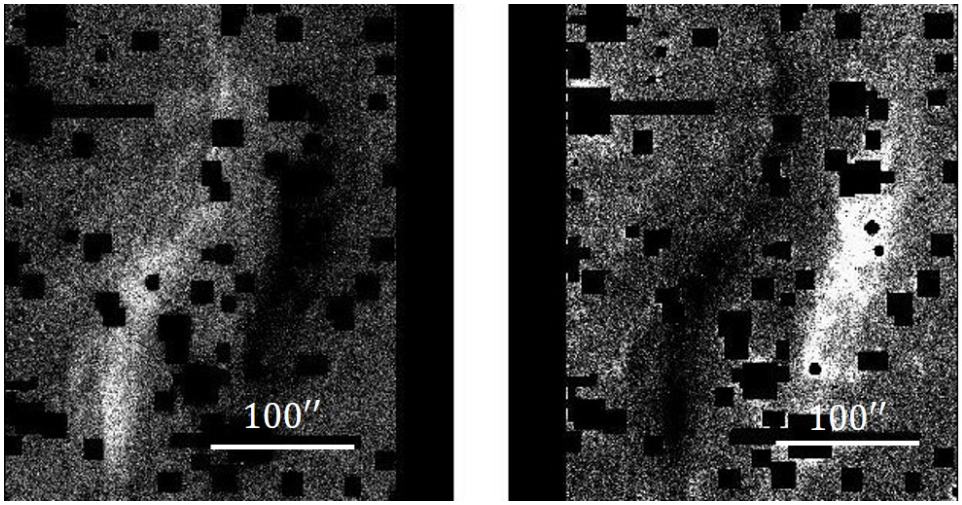

Figure 2.4: Left: The positive sub-difference-image of LE#4. Right: The negative sub-difference-image of LE#4 (after multiplying by (-1)).

2.5 Understanding Features in the Two-Dimensional Cross-Correlation of an Image Pair

After running the 2-D CC task on the difference-images, a bright horizontal line and a bright vertical line can be seen in the 2-D CC images. These features are unrelated to the LE feature. These vertical and horizontal features happen due to detector residual electronics correlations. To solve the negative effect of these issues, a region (with equal size to that of the LE region) is selected from each diffrence-image in which there is no LE feature and called the *control region*; it acts as a control case. Then, tasks 2 and 3 of Section 2.4 are completed to prepare the sub-difference-images of the control region to perform the 2-D CC. The appearance of the 2-D CC process for the control

region is like the right panel of the Figure 2.5*a*. The *cross* shape shows the distribution of the control region. Also, the intersection of the control region in the middle of the image illustrates *lag 0*, where two positive and negative sub-difference-images are covering each other completely during the 2-D CC process. Since there is not shift between positive and negative sub-difference-images and both are in equal in size, the lag 0 is located in the middle of the 2-D CC image and can be considered an *origin*. This pixel position has zero intensity in the CC image.

Next, by subtracting the control region CC sub-image from the LE region CC image, the *net CC* of the LE is obtained. Note should be taken that the pixel value range for LE and control regions should not necessarily be the same. Neglecting this factor may lead to incorrect results because the LE net CC is the result of differencing the CC of the control region image from the CC of the LE region image. This LE net CC contains the information such as the location of the maximum flux, that allows us to extract the LE apparent proper motion value in the sky with respect to the stellar objects.[2] Figure 2.5*a* illustrates the 2-D CC image from LE#4 region (Left panel) and also the 2-D CC image from control region (right panel). In Figure 2.5*b* the net CC image of LE#4 is shown. In the net CC image the defects are subtracted.

2.6 Estimating the LE APM Vector

This section describes how the LE APM can be obtained by using the CC of LE features. Each image in the focal plane of the Mosaic-1.1 imager covers approximately 0.25 square degrees of the sky. The pixel size is 0.26 *arcsec* at the 4-m telescope (See Table 1.3). By using the interval between observation times and position difference of LE features, we can obtain the LE APM in *arcsecond* yr^{-1}.

[2] This is explained further in subsequent sections of this chapter.

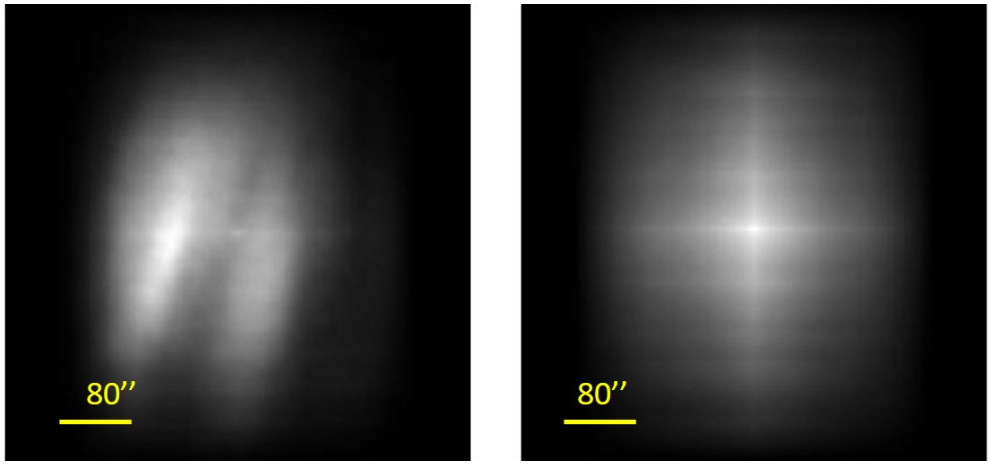

(a)

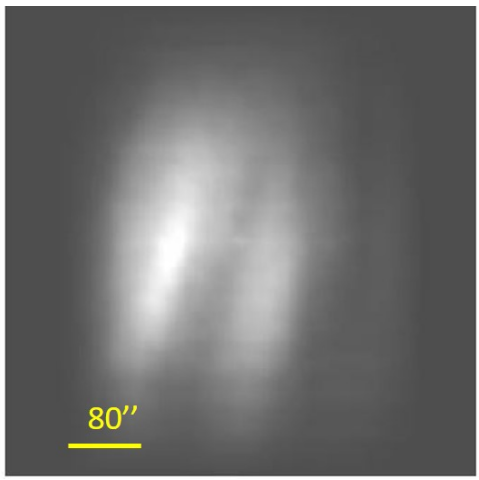

(b)

Figure 2.5: *a.* Left: The 2-D CC image of LE#4 region. Right: The 2-D CC image of control region. *b.* The net CC image, which is the result of the subtraction between two top images.

Recall that LEs are usually extended faint features. They generally have small pixel values in digital astrophotography. Therefore, artefacts and defects in the LE region image can negatively affect the analysis.

After performing tasks discussed in Sections 2.4 and 2.5, the net CC is then converted to a FITS image to check whether there is a possible LE feature or not. By using IRAF and DS9 packages for each LE difference-image sample, we compared the LE net CC image with its LE region on the difference-image. To confirm the likely peak as the LE CC, the following three steps were taken:

1. **Determining motion vectors on the LE image**

   Some bright region pairs (see Figure 3.1*a* as a sample case) should be considered on the first and second LE epochs of the LE region. Then, the displacement vector (red vectors in Figure 3.1*a*) for each of the bright point pairs should be measured. For instance, Figure 3.1*a* indicates small yellow and blue circles as bright points on the first and second LE epochs, respectively. Next, some red vectors between each appropriate pair of yellow and blue circles are considered as probable proper motion vectors. In most of the LE region difference-images, we considered more than one displacement vector from a bright point in the first LE epoch to the second LE epoch since we wanted to examine several probable LE motions.

2. **Determining motion vectors on the net cross-correlation image**

   Since both sub-difference-images (i.e., the LE region and control region images) investigated samples in this thesis are the same size and do not have any shifts, the lag 0 coordinate in the LE net CC image is equal to the size of the sub-difference-images, or the center of the net CC image. Then, the probable proper motion vectors with respect to origin is found. Consequently, these vector locations are compared to the CC maximum coordinate and its related areas (see panels *d* and *e* in Figure 3.1) to figure out the reasonable peak for the possible

LE. If not, it means that the obtained maximum CC process may not be the expected peak.

3. **Considering a special region to find the LE CC value**
   The last step performed on the LE net CC image is based on the motion vector directions in the LE region difference-image. A region in the LE net CC image is considered with respect to lag 0 coordinate which needs to be large enough to contain all of the probable proper motion vectors in the net CC image (see the thin black rectangle in the panels *d* and *e* of Figure 3.1). For the LE#2 image, the region covers columns 780 to 1100 and lines 480 to 650 (size: 320×170). The maximum CC value for this chosen region is estimated as the LE CC value. Obviously, considering this special region on the LE net CC image means that the 2-D CC maximum result is not the expected LE CC value. The main reasons for this discrepancy could be the closeness of the pixel value ranges between the LE and control regions in most of the cases (see Tables 3.9 and 3.10) as well as the existence of the different dust clump shapes.

2.7 Technique Used to Determine the LE APM Uncertainty

In this thesis, CC is used to find an appropriate value close enough to the peak value of the LE proper motion. The half-peak intensity is taken as the threshold above which the values are not affected by artefacts or backgrounds. This means that the FWHM method is used to estimate the threshold for the net value of the LE proper motion magnitude's 2-D CC.

2.7.1 FWHM Method

The following section discusses the use of the FWHM method to find the uncertainty for one-dimensional and two-dimensional approaches, respectively.

Univariate Normal Distribution

A one dimensional (1-D) Gaussian distribution is given by:

$$p(x) = \frac{1}{\sqrt{2\pi}\sigma} exp(\frac{-(x-\mu)^2}{2\sigma^2}) \tag{2.5}$$

where $\frac{1}{\sqrt{2\pi}\sigma}$ is the normalization constant, μ is the *mean* value, and σ is the *standard deviation* indicating the spread of the measured value. Standard deviation is given by:

$$\sigma = \sqrt{\frac{1}{N}\sum_{i=1}^{N}(x_i - \mu)^2} \tag{2.6}$$

where index i indicates the observed sample values and N shows the sample size. For a Gaussian distribution, about 68% of the data values fall within one standard deviation of the mean (mathematically, $\mu \pm \sigma$), about 95% within two standard deviations ($\mu \pm 2\sigma$), and about 99.7% within three standard deviations ($\mu \pm 3\sigma$). Equation 2.7 shows the relation between the FWHM and the standard deviation:

$$FWHM = 2\sqrt{2ln2}\sigma = 2.355\sigma. \tag{2.7}$$

Thus, based on the Equations 2.5 and 2.7, approximately 76% of the data values lie within the 1.1775σ of the mean.

Multivariate Normal Distribution

A multivariate normal (or Gaussian) distribution is a generalization of the 1-D normal distribution to higher dimensions. In this thesis, a 2-D Gaussian distribution is used as a special case of the multivariate normal distribution, and the cross section of the bivariate Gaussian distribution is an ellipse.

Similar to the univariate normal distribution, the multivariate normal distribution equation is given:

$$p(\overrightarrow{x}; \overrightarrow{\mu}, \Sigma) = \frac{1}{(2\pi)^{\frac{n}{2}}|\Sigma^{\frac{1}{2}}|} exp(\frac{-1}{2}(\overrightarrow{x} - \overrightarrow{\mu})\Sigma^{-1}(\overrightarrow{x} - \overrightarrow{\mu})^T) \tag{2.8}$$

where $\overrightarrow{x}$ is a vector with n values, $\overrightarrow{\mu}$ is a vector with length n as a mean for distribution, Σ is the covariance matrix, and $|\Sigma|$ is the matrix determinant. The term in front of the exponential is the constant coefficient, and $(\overrightarrow{x} - \overrightarrow{\mu})$ and $(\overrightarrow{x} - \overrightarrow{\mu})^T$ are row and column vectors, respectively. For a bivariate Gaussian distribution n is equal to 2. If a single cut is taken from the bivariate normal distribution at some probability, then it can be plotted as a contour plot, called an isocontour. The contour of constant probability would look like an ellipse for a bivariate Gaussian distribution. The mean vector $\overrightarrow{\mu}$ is the two-dimensional point showing the center of the ellipse and Σ shows the spread or deviation from the mean vector $\overrightarrow{\mu}$. Arrays of Σ contain standard deviation values from the mean value in x and y directions in the case of a bivariate Gaussian distribution and also demonstrate the relation between these deviations.

2.7.2 Shapes of Contours

Depending on the ratio of the standard deviations in the x and y directions, there are different shapes of contours produced. There are two cases: (a) Σ is a Diagonal Matrix and (b) Σ is a Non-Diagonal Matrix.

In the first case, Σ is a diagonal covariance matrix which shows that Σ has an axis-aligned ellipsoidal shape that depends on diagonal members. If the diagonal member values are not equal to each other, the ellipse will be axis-aligned in the direction in which the diagonal member has a larger value and the spread in that direction will be larger than the spread in the other direction with a smaller value for the diagonal member. If diagonal members are equal to each other, then the spread in both directions will be the same and the contour shapes will be circles.

In the second case, the covariance matrix is not diagonal for the multivariate Gaussian distribution. Then, the contours of the bivariate Gaussian distribution will be rotated ellipses. Figure 2.6 shows contours produced with a non-diagonal Σ matrix for a typical bivariate Gaussian distribution.

Parametric representation tilted ellipse equations:

In the *parametric* representation, when Σ is not a diagonal matrix, an ellipse is parametrized by $(h\ ,\ k)$, a, b, and τ, which indicate the ellipse center, its semi-major, its semi-minor, and its tilt angle in radians, respectively. The parametric presentation equation is given by:

$$\frac{(x-h)^2}{a} + \frac{(y-k)^2}{b} = 1. \tag{2.9}$$

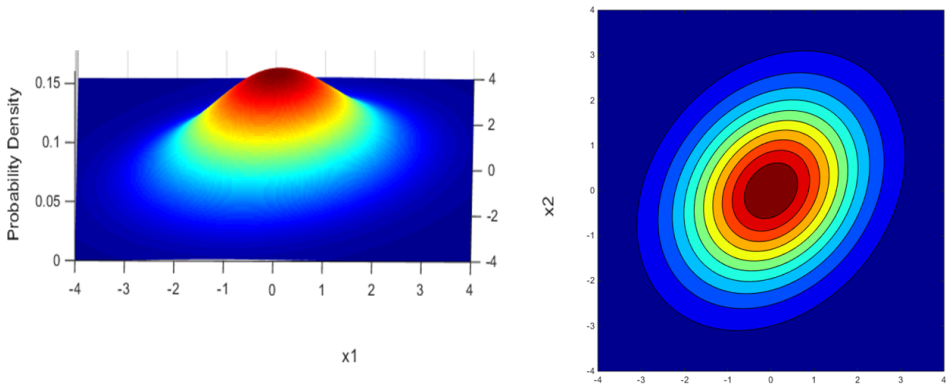

Figure 2.6: Left: A typical rotated bivariate Gaussian distribution. Right: Contours of the bivariate Gaussian distribution (left image) with non-diagonal σ matrix.

Equation 2.9 contains a set of points $(x(t), y(t))$ where

$$x(t) = h + a\cos(\tau)\cos(t) - b\sin(\tau)\sin(t) \tag{2.10}$$

$$y(t) = k + a\sin(\tau)\cos(t) + b\cos(\tau)\sin(t). \tag{2.11}$$

Here, $0 \leq t \leq 2\pi$ and τ is the counter-clockwise rotation of the ellipse in radian.

2.7.3 FWHM Method In Use

When the maximum of the CC of the LE features is found, the uncertainty of the LE APM can be estimated. In order to do this, first, the bivariate Gaussian distribution of the LE CC is used based on plotting the intensity versus the image coordinates. Thus, the peak of the 2-D CC is actually the maximum intensity of the net CC image.

Then, by using bivariate Gaussian distribution and the FWHM method, the half-peak intensity and, consequently, the related largest contour to this half-peak intensity are automatically found in the code.

Finding the half-peak largest contour intensity is a critical task, because any mistake in determining the half-height of the maximum peak leads to significant errors in the method. Performing 2-D CC between positive and negative sub-difference-images, it is expected that the CC peak is only due to the LE features. However, even by considering all the aspects of the difference-imaging process, there may still exist some unexpected artefacts in the difference-images that can negatively affect the CC result (i.e., the peak). Considering the three-dimensional contour of the bivariate Gaussian distribution of the LE CC, it can be seen whether or not any artefacts have affected the maximum of the LE CC. If there are artefact peaks, then their height should be subtracted from the LE CC peak height (in the next chapter you will see that this task is performed for LE#4). However, this may lead to having an underestimated uncertainty. After running this task, the LE maximum peak half-height can be re-evaluated. Next, the largest contour in the half-height is found and a tilted ellipse fitted to that contour by using the method of least squares. Since the general contour shape for a bivariate Gaussian distribution is a tilted ellipse, it is fitted to the largest contour in the half-height of the LE 2-D CC.

As mentioned before, in the parametric ellipse Equations (Equations 2.10 and 2.11), the ellipse center, $(h\ ,\ k)$, shows the shift of the LE 2-D CC peak with respect to lag 0 in the x and y directions. Thus, $(h\ ,\ k)$ leads to finding the best estimate of the apparent proper motion between the two LE epochs. Also, a and b are semi-major and semi-minor axes of the tilted ellipse. Here, semi-major a does not have any physically useful information, since it is along the illuminated dust filament and we do not know how far it is distributed. In contrast, semi-minor b and angle τ contain important information because they indicate: (a) the LE proper motion uncertainty (or the

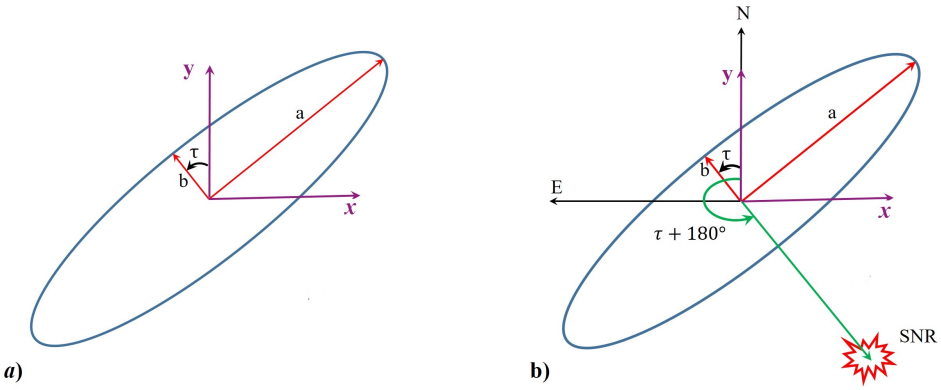

Figure 2.7: In both schematic, tilted ellipses indicating the LE proper motion uncertainty with semi-minor axis b and the angle τ in direction of the LE motion with respect to the y-direction (panel a) or angle $\tau + 180°$ in the direction of the LE movement away from the supernova remnant (SNR) (panel b). The green vector in panel b is toward the SNR. Additionally, vectors N and E show the north and east directions in the sky, respectively.

maximum error: i.e., half value of the FWHM) and (b) the approximate direction of the LE motion with respect to the y-direction (see τ in Figure 2.7a) or direction of the LE motion far away from the source event coordinate, with respect to the north and east, respectively (see ($\tau + 180°$) Figure 2.7b).

2.7.4 Estimating the LE APM Vector Uncertainty

Up to now, this section has explained how the half-peak of the brightness intensity in the LE net CC image was found and then the largest contour of this height obtained (see Section 2.7.1). A code was developed in MATLAB to get the best-fit ellipse for the largest contour (see Section 2.7.2). The least square technique was used to find the best-fit ellipse. In general, the ellipse is tilted and the parametric representation was chosen for its equations in this study. Equations 2.10 and 2.11 were used to find the best-fit ellipse. These equations consisted of five parameters, a, b, h, k, and τ representing the semi-major axis, semi-minor axis, coordinate of the ellipse center,

and the tilted angle of the ellipse, respectively. Parameters are calculated with 95% confidence bounds using the method of least squares. In section 2.7.3, the astrophysical interpretation of these five parameters was given.

After performing all the mentioned steps to find the maximum LE CC and its uncertainty, the LE APM and its uncertainty can be obtained. Each image in the focal plane of the Mosaic-1.1 imager covers approximately 0.25 square degrees of the sky. The pixel size is 15 $\mu m = 0.26$ *arcsec* at the 4-m telescope (see Table 1.3). By using the interval between observation times and position difference of LE features, we can obtain the LE APM in $arcseconds\ yr^{-1}$.

This chapter explained the method used to find the APM of LE features as well as its uncertainty on the sky between two observation times. In the next chapter, the general results from this study will be explained. Then, characteristics of each difference-image used in this work and their results will be discussed individually.

Chapter 3

Results: Light Echo Proper Motion

In this study, ten difference-images of LE features, of size 2048×4096 *pix* (see Section 1.3, Table 1.3), were chosen from the fields in the vicinity of the Tycho and Cas A supernova remnants (SNRs). Although the number of studied difference-images is not large, the selected number of images is appropriate to investigate the CC method since difference-images were picked to be a sample of forms discovered to be or suspected of being LEs.

In this chapter, the general obtained results will be reported first, then the difference-image characteristics and the outcomes will be described for each individual difference-image used in this study.

3.1 Results

In this section, the results based on the application of the 2-D CC method using the best-fit ellipse (to find the APM vector and its uncertainty) are described.

We adopted the Cas A and Tycho SNRs coordinates derived from the radio maps (Rest

et al., 2008; Green, 2014) in our study. Table 3.1 represents the Cas A and Tycho SNRs, positions in the Equatorial Coordinate System (J2000.0). Also, we adopted the year of outburst event for Cas A to 1681 AD (Fesen et al., 2006) and consider the outburst event for Tycho to be 1572 AD as reported by Tycho in that year (Stephenson & Green, 2002).

Table 3.1: Cas A and Tycho remnants J2000.0 coordinates

SNR	RA (hh:mm:ss)	Dec (deg:mm:ss)
Cas A	23 23 24	+58 48 54
Tycho	00 25 08	+64 09 56

Table 3.2 provides details regarding the ten LEs and their APM vectors. The LEs are indicated by a running number in column one. The second column represents the related SNR for each LE. The interval of time between the two observational epochs for each LE is shown in the third column.

Recall, additional LE properties are provided in Table 2.1. Column four gives the estimated APM magnitude for each selected LE in $''yr^{-1}$. Position angles (PA), τ, in degrees are given in column five. The position angle is measured as a tilted ellipse fit to the half-peak largest contour of the LE CC. Column six presents the PA in degrees measured with respect to the mid-point between the LE features and their related SNR coordinates, for the APM. The last column in Table 3.2 shows previously measured PAs from Rest et al. (2008) and (2011), in instances where they exist. Results will be compared and discussed in Sections 3.2 and 3.3.

Table 3.2: Light Echoes and their associated parameters and Apparent Proper Motion vectors

LE number	SNR	Interval (in years)	APM[1] ± APM(stdev)[2] arecsec/year	PA[3] ± PA(stdev)[4] degrees	PA[5] degrees	Previous Measurement degrees
LE#1	Cas A	2.25	30.7 ± 16.7	199 ± 3	296	299.10[6]
LE#2	Cas A	1.93	32.4 ± 7.6	343.5 ± 3.5	338	-
LE#3	Cas A	1.93	20.0 ± 4.6	286 ± 6	292	-
LE#4	Cas A	1.93	46.3 ± 8.0	251.5 ± 2.5	257.3	245[6]
LE#5	Cas A	3.95	56.0 ± 11.2	231 ± 6	257.4	-
LE#6	Tycho	1.93	24.3 ± 14.3	162.5 ± 7.5	188	-
LE#7	Tycho	1.93	11.2 ± 2.0	180 ± 5	190	-
LE#8	Tycho	1.93	12.0 ± 1.7	345 ± 10	355	-
LE#9	Tycho	2.90	38.6 ± 8.2	339 ±5	321	-
LE#10	Tycho	1.15	33.7 ± 7.6	141 ± 2	137	135.5 ± 17.1[7]

(1): Apparent proper motion magnitude in $''yr^{-1}$. (2): Standard deviation of the apparent proper motion magnitude in $''yr^{-1}$.(3): Position angle (PA) in degrees; shows the best-fit ellipse angle to the half-peak largest contour of LE CC. (4) Standard deviation of the position angle, PA(stdev) in degrees, show the size of deviation from the best-fit ellipse angle to the half-peak largest contour of LE CC. (5): Position angle with respect to mid-point between LE features and their related SNR coordinates, the direction of the LE motion far away from the source event coordinate, east from north. (6): Rest et al. (2011).. (7): Rest et al. (2008).

Based on the obtained APM magnitudes and directions, their relative uncertainties have been calculated. The estimations are provided in two separate tables for Cas A and Tycho LEs. All studied cases present the correlation of the time interval and the shape of the scattered dusts with the obtained relative uncertainty. Table 3.3 and Table 3.4 suggest that increasing the interval between the LE epochs leads to an increase in the uncertainty due the dust not being uniform and the chance of different scattered dust existing from different echo depths increases. Also, dust clump shapes are obviously different from the ideal near-parallel shape of dust filaments.

Table 3.3: APM and PA relative uncertainties for Cas A LEs

LE number	Interval (yr)	APM uncertainty (%)	PA uncertainty (%)
LE#1	2.25	55	6
LE#2	1.93	23	2
LE#3	1.93	23	4
LE#4	1.93	17	2
LE#5	3.95	20	5

Table 3.4: APM and PA relative uncertainties for Tycho LEs

LE number	Interval (yr)	APM uncertainty (%)	PA uncertainty (%)
LE#6	1.93	59	9
LE#7	1.93	18	6
LE#8	1.93	14	6
LE#9	2.9	21	3
LE#10	1.15	23	1

Knowing the SN distance, its age (here, in the studied cases, time interval between the outburst event and the first LE epoch is considered for each sample), and separation angle between the mid-point between two LE epochs and the SNR led us to obtain the echo depth, z, for each LE difference image and also the expected APM for that echo depth, z, does not depend on inclination.

Table 3.5: Cas A LE APMs and their physical characteristics

LE number	Estimated APM in this thesis ($''yr^{-1}$)	z (pc)	APM for z ($''yr^{-1}$)	Expected probable inclination (α) range (degree)
LE#1	30.7 ± 16.7	-4.52	18.6	-30.1 — +17.3
LE#2	32.4 ± 7.6	202.55	26.5	-37.2 — +8.8
LE#3	20.0 ± 4.6	121.95	23.0	-6.8 — +42.5
LE#4	46.3 ± 8.0	629.12	44.4	-34.0 — +30.3
LE#5	56.0 ± 11.2	630.51	44.5	-51.3 — -1.7

Table 3.6: Tycho LE APMs and their physical characteristics

LE number	Estimated APM in this thesis ($''yr^{-1}$)	z (pc)	APM for z ($''yr^{-1}$)	Expected probable inclination (α) range (degree)
LE#6	24.3 ± 14.3	-43.41	30.8	-6.8 — +50.8
LE#7	11.2 ± 2.0	-42.21	30.5	+40.20 — +54.0
LE#8	12.0 ± 1.7	31.62	28.3	+52.2 — +64.7
LE#9	38.6 ± 8.2	174.14	35.6	-24.5 — +18.0
LE#10	33.7 ± 7.6	166.56	35.2	+16.1 — +31.9

On the other hand, obtaining the echo depth, z, and the estimated LE APM magnitude for the same echo depth contributed to finding the probable inclinations for the scattered dust in the same echo depth in the line of sight. All the calculations and results are summarized in Table 3.5 for Cas A probable LEs and in Table 3.6 for Tycho LEs, separately. From these tables, it can be seen that the estimated APM magnitude from the study is consistent with the expected APM magnitude with zero inclination for the expected echo depth within 1σ, except for LE#7 and LE#8. LE#7 is predicted to have 46.4° angle with the echo depth of the size of 31.62 pc behind the source event in the line of sight. LE#8 is predicted to have 58.7° with the echo depth of the size of 31.62 pc in front of the source event in the line of sight.

3.1.1 Goodness of Fit

The R–squared value, root-mean-square deviation (RMSD), as well as the normalized root-mean-square deviation (NRMSD) were employed to evaluate the goodness of fit for each LE sample in this study. As we know from general statistical knowledge, R–squared lies between zero and one. Zero value indicates that there is no correlation between the best-fit ellipse and the observational largest contour at half-peak. In contrast, when R–squared equals one, the best-fit ellipse perfectly fits the data.

Considering a 95% confidence interval, best-fit ellipses lies within $f(x_i) \pm 2\text{RMSD}$. Therefore, the lowest RMSD (9.73) belongs to LE#4 and the highest RMSD is 48.42 calculated for LE#5 among the Cas A LEs. These two LEs have the same first LE epoch; however, the interval of LE#4 is about half of that of LE#5. The shorter interval results in a better goodness of fit. The LE#10 difference-image has a 1.15 yr interval and LE#9's has a 2.9 yr interval. Both have near-parallel shaped features. However, it can be seen from Table 3.8 that the RMSD value for LE#9 is about 2 times that of LE#10. The other three probable LEs of SNR Tycho, LE#6, LE#7, and

Table 3.7: Goodness of the fit for the Cas A LEs' APM

LE	R^2	RMSD	NRMSD (%)
LE#1	0.963	13.52	1.8
LE#2	0.924	10.86	4.0
LE#3	0.981	12.12	3.5
LE#4	0.996	9.73	1.9
LE#5	0.907	48.42	7.6

LE#8, have the same time interval. Yet LE#6 and LE#8 do not have near-parallel LE features, LE#8 has clumpy dust, and the APM on the difference-image is small with respect to the time interval.

Table 3.8: Goodness of the fit for the Tycho LEs' APM

LE	R^2	RMSD	NRMSD (%)
LE#6	0.973	17.24	3.9
LE#7	0.926	3.72	4.5
LE#8	0.941	2.29	4.1
LE#9	0.978	10.42	2.7
LE#10	0.997	5.25	1.0

Normalized root-mean-square deviation (NRMSD) is used to make the RMSD dimensionless, so this value can be stated as a percentage. Lower NRMSD indicates less RMSD. The RMSD value is normalized to the maximum difference between data points, thus it can make it easier to compare the largest contour at half-peak and the best-fit ellipse with different scales. Tables 3.7 and 3.8 reveal that amongst the

samples, LE#10 has the lowest NRMSD and LE#5 has the highest. Again, it must be noted that the NRMSD alone cannot be enough to evaluate the goodness of fit. For instance, both LE#1 (2.25 yr) and LE#8 (1.93 yr) have the scattered clumps of dusts on their difference-images; however, the NRMSD for the former is less than the latter.

It can be concluded that since the shapes of LE features and their time intervals lead the half-peak largest contour to have various shapes, each of the mentioned goodness-of-fit methods are not individually sufficient to understand the reliability of the results. So, we need to consider all three goodness-of-fit methods together to decide the reliability of the fit. If a sample has a high R–squared value and low RMSD and NRMSD values then the fit is reliable, such as is the case with LE#3, LE#4, LE#9, and LE#10.

In the next two sections (3.2 and 3.3), all ten LE difference-images are discussed, and the following items have been explained and discussed in detail:

1. **Characteristics of each LE difference-image**
2. *Process of obtaining APM*
3. **Discussion and comparison with other researchers' results**

Since the approach for calculating the APM vector is the *same* for all ten LE difference-images, 'Process of obtaining APM' is described for *the first two LEs* (LE#1 and LE#2) and is *not* presented for the rest of the LE difference-images (i.e., LE#3 to LE#10).

3.2 Sample Light Echo Features for Cas A SN

In this section, for individual Cas A LEs, LEs from LE#1 to LE#5, the LE feature characteristics and the result of probable LE APM vectors are described in detail. As mentioned before, only for LE#1 and LE#2, the 'Process of obtaining APM' is described in this section. All of the locations, the size of selected sub-difference-images, and pixel value ranges for both LE and control regions are shown in Table 3.9 for all probable Cas A LE difference-images.

Table 3.9: Location, image size, and pixel value ranges of Cas A LEs

LE number	LE Location w.r.t. Cas A	Possible related LE region image size	LE region pixel value range	Control region pixel value range
LE#1	north west	846×562	-40 — +20	-20 — +20
LE#2	north west	1146×684	-60 — +50	-60 — +50
LE#3	south east	1000×1450	-120 — +105	-120 — +105
LE#4	east	870×1126	-160 — +115	-40 — +40
LE#5	east	1330×1304	-50 — +30	-50 — +30

3.2.1 LE#1

1. LE#1 is the most complicated LE feature among the 10 selected LE sample images. The LE features at first and second epochs are spread out over all parts of the image. There are more than one near-parallel LE feature in each epoch (see Figure 3.1a). In other words, Figure 3.1a presents some dust clumps which may be related to more than one echo depth, z, along the line of sight. Also, there are some small black and

white regions with pixel values comparable to LE pixel values, in the vicinity of LE features in Figure 3.1*a* that needed to be masked.

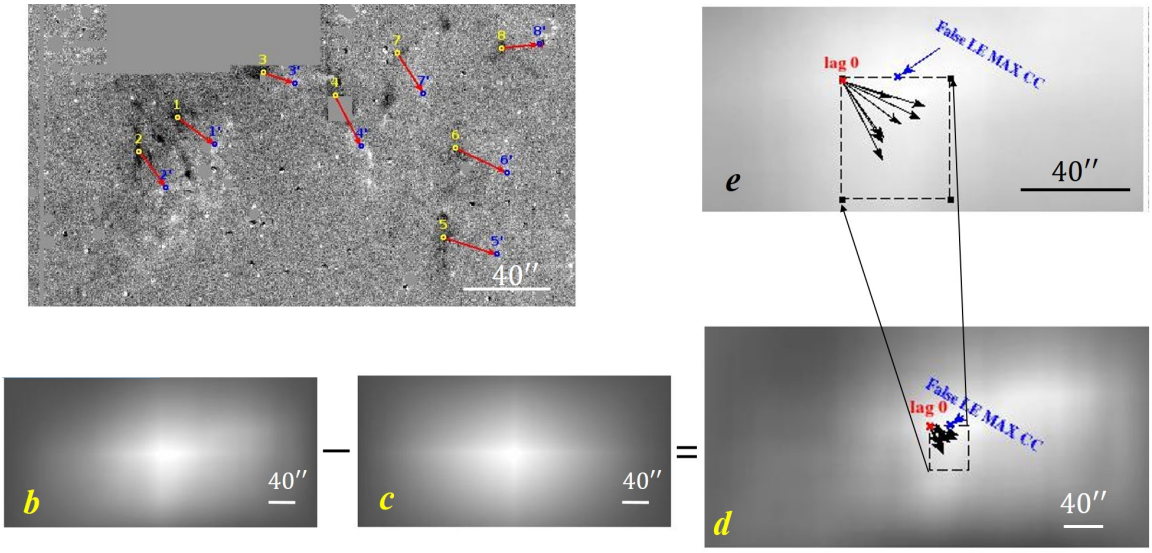

Figure 3.1: *a.* The LE#1 difference-image. The masked areas are appeared as bright gray rectangles with zero pixel values. *b.* The 2-D CC image of the LE region sub-difference-image. *c.* The 2-D CC image of control region sub-difference-images. *d.* The net CC image is a result of the subtraction between *b* and *c* images. The black box indicates the region where finding the LE#1 2-D CC maximum is probable. Vectors in the black box show the motion vectors demonstrated in *a.* The large blue vector shows the false LE#1 2-D CC maximum. *e.* The magnified black box and its neighbourhood from the image *d.*

2. The 2-D CC process was done for each of the sub-difference-images (see Figure 3.1*b* and 3.1*c*). Then, the CC image of the control region sub-difference-image was subtracted from the CC image of the LE region sub-difference-image to get the net CC image (see Figure 3.1*d*). When the distance between lag 0 and the LE CC peak on the net CC image (in Figure 3.1*d*) was compared with the distance between the LE epochs on the difference-image (Figure 3.1*a*), we found that the distance on the net CC image is longer than the distance between LE epochs. This means that the obtained CC

peak is not a reasonable peak for the possible LE. To solve this issue, eight red motion vectors between two LE epochs were found (see Figure 3.1a) as described in Section 2.6. Then, a region was examined to cover all the motion vectors on the net CC image to find the probable LE CC. Figure 3.1e is the magnified area of the region and its neighbourhood.

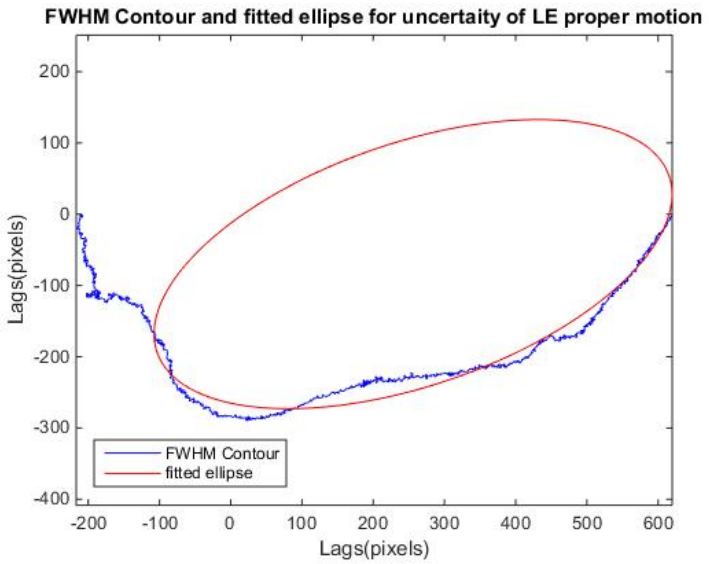

Figure 3.2: Fitted ellipse with tilt angle = 199° to the half-peak largest contour of the LE#1's 2-D CC.

3. The APM magnitude and tilted angle for LE#1 had relative uncertainties of about 55% and 6%, respectively (see Table 3.2 and Figure 3.2). Our measurement, including 1σ uncertainty, was $(31 \pm 17)\ ''yr^{-1}$, and the expected APM magnitude according to Rest et al. (2008) was in the range (20 - 40) $''yr^{-1}$. The APM magnitude uncertainty shows that the obtained value was not well-determined (see Table 3.5).

3.2.2 LE#2

1. Figure 3.3 shows the image of LE#2. The image indicates that the Point Spread Function (PSF) wings were not large enough in the original masking process. Also, there are lots of small obvious white and black areas that are not related to the LE features, but have pixel values comparable to the pixel values of the LE feature. Thus, an intense masking process was conducted on the LE image.

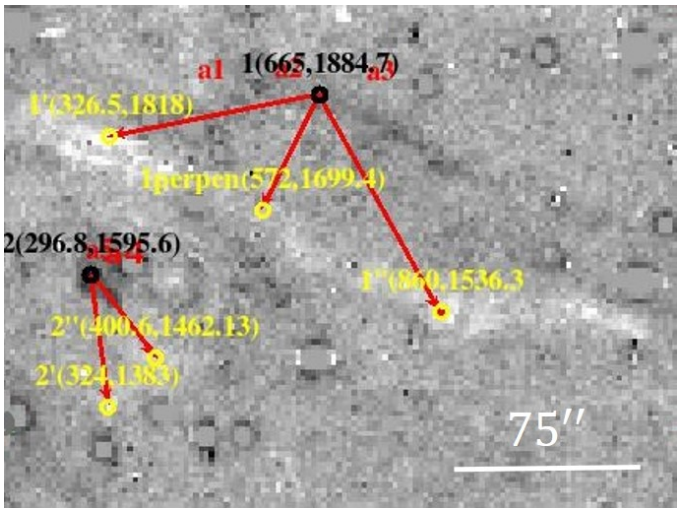

Figure 3.3: LE#2 sub-difference-image shows that the PSF wings are not large enough to mask the saturated areas. Also, the small black and white areas indicate that they are not relevant to LE features are evident. Red vectors represent the motion of the bright points between two LE features.

2. When the CC process was conducted for the LE#2 image, the presence of the control region could be detected in the LE CC image (see the top-left panel in Figure 3.4). To eliminate this negative effect on the LE CC image, an image of 1146×684 *pix* was chosen from a control region of the original difference-image. Then, the CC of this image was obtained (see the top-right panel in Figure 3.4). After subtracting these two CC images from each other, the net CC image of LE#2 was obtained, which shows

that the obvious effect of the control region had been eliminated (see the bottom panel in Figure 3.4) although because the pixel value range was the same for LE and control regions, some horizontal and vertical patterns in the net CC image remain. Comparing the displacement vectors on the LE#2 difference-image with the LE#2 CC peak on the net CC image shows that the maximum (MAX) obtained from the CC of LE#2 is not reasonable for measuring the LE proper motion. To find the LE CC value, the three-step solution discussed in the Section 2.6 was performed.

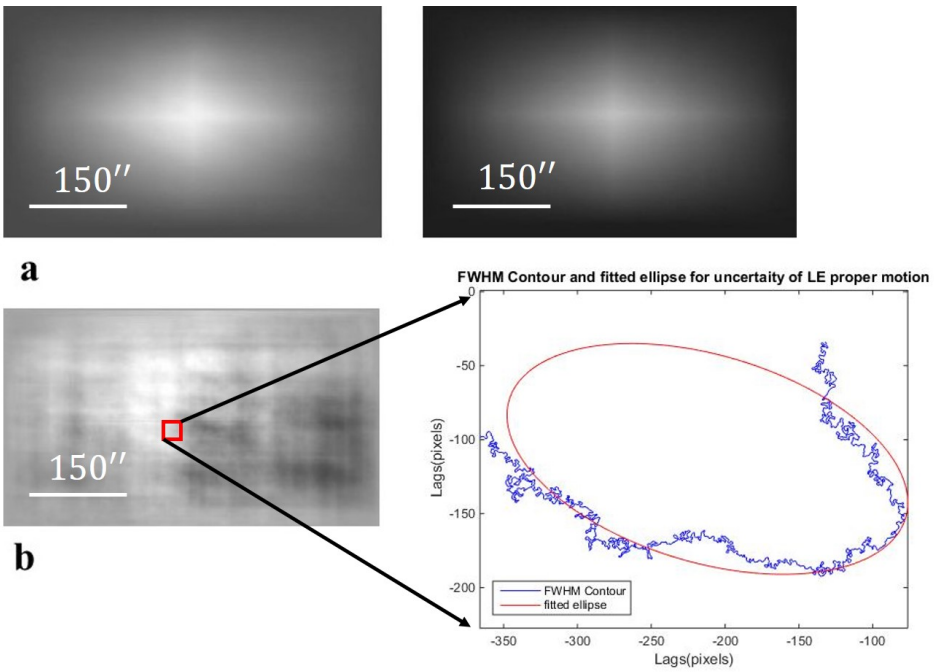

Figure 3.4: (a): Left: The 2-D CC for the LE#2 region. Right: The 2-D CC for the section of the LE#2 image without obvious LE features; this is the control region. (b): The net CC image which is the result of the subtraction between two top images.

3. After performing the corrections and three-step solution, we obtained the APM magnitude $(32.4 \pm 7.6)\ ''yr^{-1}$ (see Table 3.2 for LE#2). Table 3.5 indicates that our measurement within 1σ covers the APM value $(26.5\ ''yr^{-1})$ for the expected echo

depth, z. We also measured the PA equal to $343.5° \pm 3.5°$ with 2% relative uncertainty (see Table 3.2 for LE#2). This result is, within 1σ uncertainty, comparable to the PA that resulting from calculating with respect to the best midway of LE features and their related SNR coordinates (see column 5 of Table 3.2 for LE#2), or 338°. However, our estimated PA for LE#2 was slightly higher than the column 5 result from Table 3.2 for this LE. In Figure 3.3, the first and second epochs have two parallel filament structures and each of the epochs show a dust clump on the left. What can be said for this case, again, is that the non-uniformity of the interstellar dust may have led to a poorly determined APM.

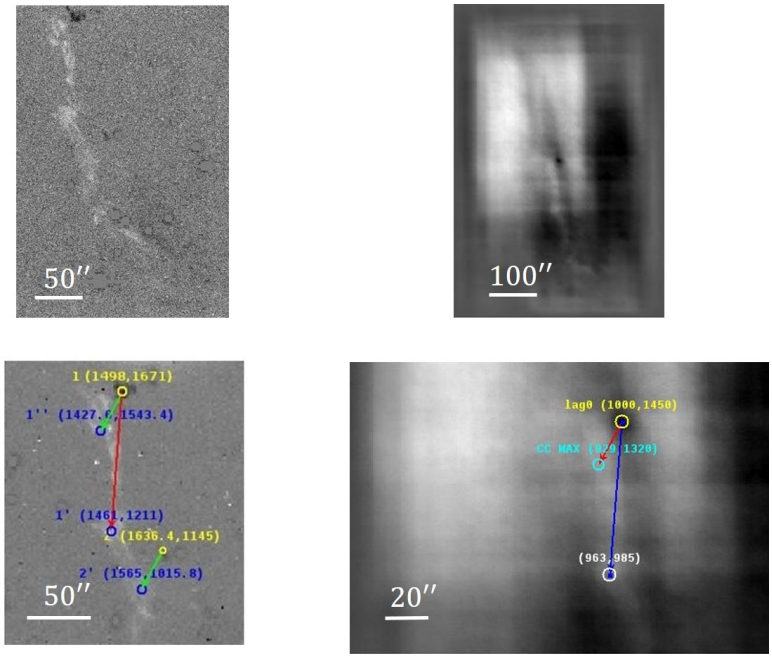

Figure 3.5: Top: LE#3 difference-image and its net CC image. Bottom: The same images as shown in the top panel but zoomed to show the motion vectors in the images.

3.2.3 LE#3

Figure 3.5 shows the difference-image of LE#3 in the top-left panel. The masking process appears to have been correctly completed and did not need to be re-run.

One important issue for this difference-image is that the first LE epoch is located in three regions (top-center, central, and bottom-center) within very small areas, and only the region located at the top center had noticeably high pixel values. In contrast, the second LE epoch is quite extended and bright throughout. Thus, the net CC image of LE#3 shows a narrow line similar to the second LE epoch from the center to the bottom of the image (see the top-left image in Figure 3.5).

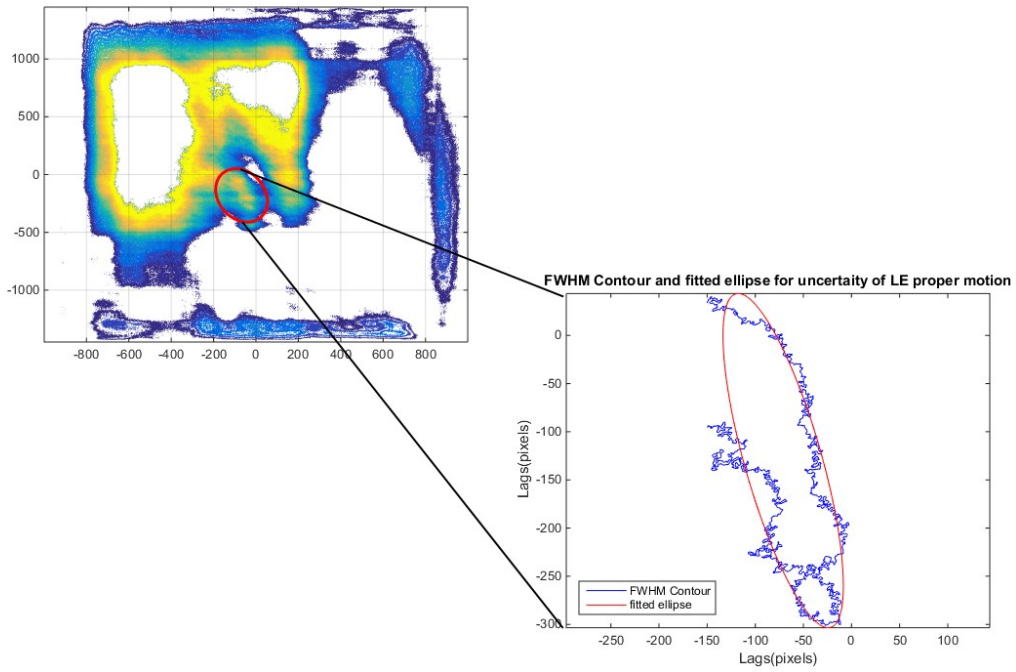

Figure 3.6: Left: The 2D CC contour image of LE#3. The red ellipse presents the area in which it is possible to find the LE CC and its best-fit ellipse. Right: The largest contour of the half-peak and its best-fit ellipse for LE#3.

Since the two LE epochs are noticeably different in size, pixel values, and their narrow features, the pixel values of the control region had a significant negative effect on the net CC image. All of these factors led to a difficult to interpret LE CC image.

Figure 3.6 shows the figure of the 2-D CC contour for LE#3 (left panel) as well as the best-fit ellipse to the half-peak largest contour (right panel), which gives the LE CC and the APM vector with its related uncertainty (see Table 3.2 for the APM vector properties of LE#3). It can be seen from Table 3.2 for LE#3 that the APM magnitude had 23% and the position angle had 4% uncertainty values. This result is consistent within 1σ uncertainty with the APM value of the expected echo depth, z, (see Table 3.5).

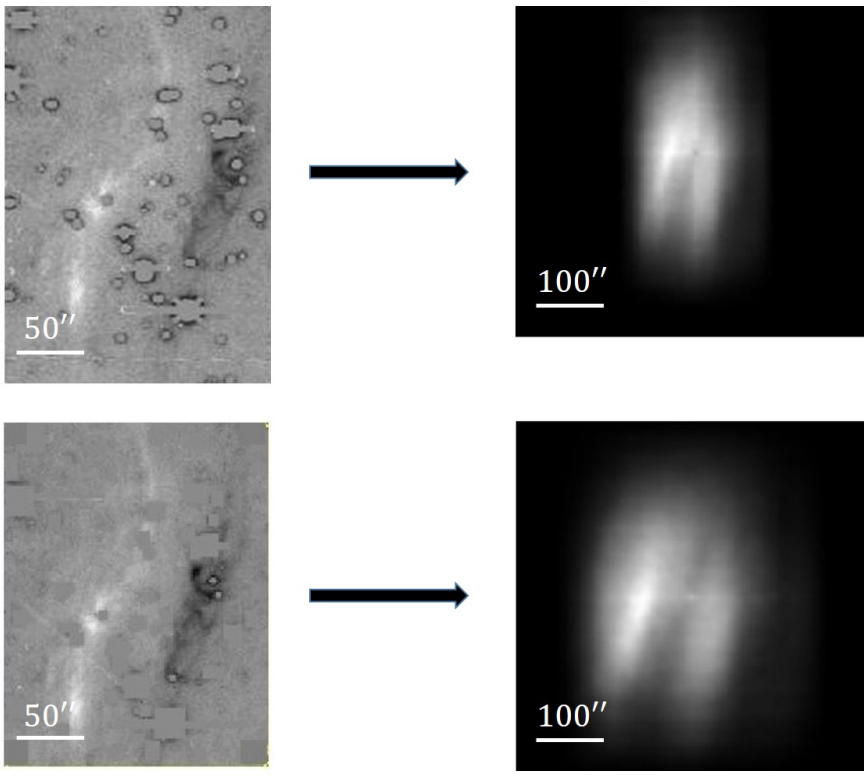

Figure 3.7: The LE#4 difference-image and its CC image before (top images) and after masking (bottom images). The bottom CC image of LE#4 shows that the masking process obviously reduced the control region's negative effect.

3.2.4 LE#4

Rest et al. (2011) discovered LE#4 located at 2000 ly in front of Cas A SNR on September 16, 2009 (in UT dates). They estimated that the LE#4 APM magnitude is about 30 $''yr^{-1}$ with a position angle equal to 65.08° (Rest, Foley, et al., 2011).

LE#4 is strong in both the first and second epochs. The LE#4 difference-image and its CC image before and after the intense masking process are represented at the top and bottom of Figure 3.7, respectively. It is evident that the masking process reduced the defects significantly.

Figure 3.8 shows the 2-D CC contour for LE#4 (left) and the best-fit ellipse to the half-peak largest contour (right). As the right panel of Figure 3.8 demonstrates, analyzing the half-peak by eliminating the effect of the peak irrelevant to the LE feature (see the right peak in the top and bottom-right panels of Figure 3.7), led to a smaller uncertainty, so it is possible it is underestimated. However, we completed the analysis of the half-peak by eliminating the effect of the peak irrelevant to the LE feature.

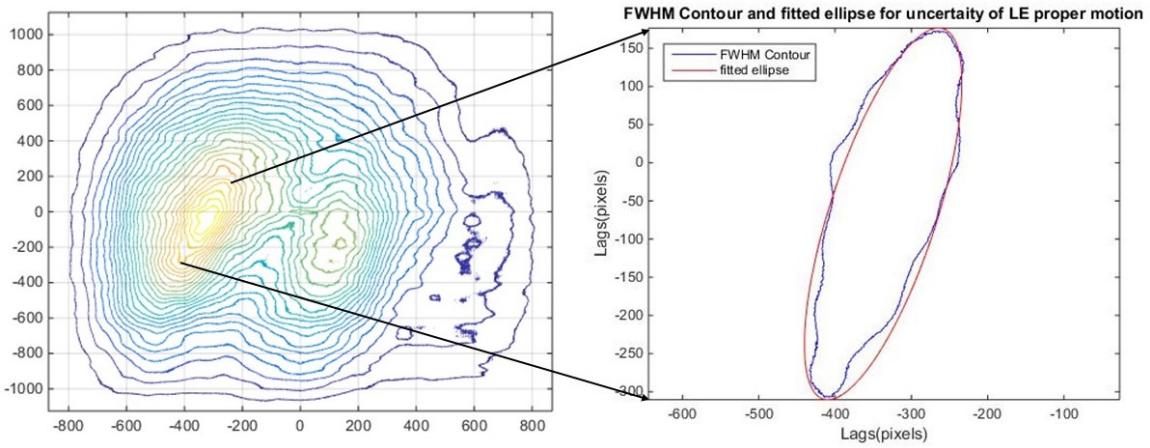

Figure 3.8: Left: The 2D CC contour image of LE#4. Right: The largest contour of the FWHM and its best-fit ellipse for LE#4.

The best-fit ellipse was used to determine the APM and PA magnitudes and their uncertainties. Table 3.2 indicates that there was about a 17% and a 2% uncertainty for the LE#4 APM magnitude and PA, respectively. Comparing the APM value from the LE CC process ($46.3 \pm 8.0\ ''yr^{-1}$) with previous research by Rest et al. (2011) reveals that there is a good agreement between the results, since Rest et al. (2011) reported the APM value of this LE to be about $(30 \pm 10)\ ''yr^{-1}$. Moreover, the average value of the APM magnitude was consistent with, though a bit higher than, the APM value ($44.4\ ''yr^{-1}$) for the expected echo light in our line of sight. Comparing the PA result of the current research ($(251.5 \pm 2.5)^\circ$) with Rest et al.'s work in 2011 (245°) shows that the obtained result was 8.5% closer to the PA calculated with respect to the mid-point between the LE features and the SNR, Cas A (257.3°).

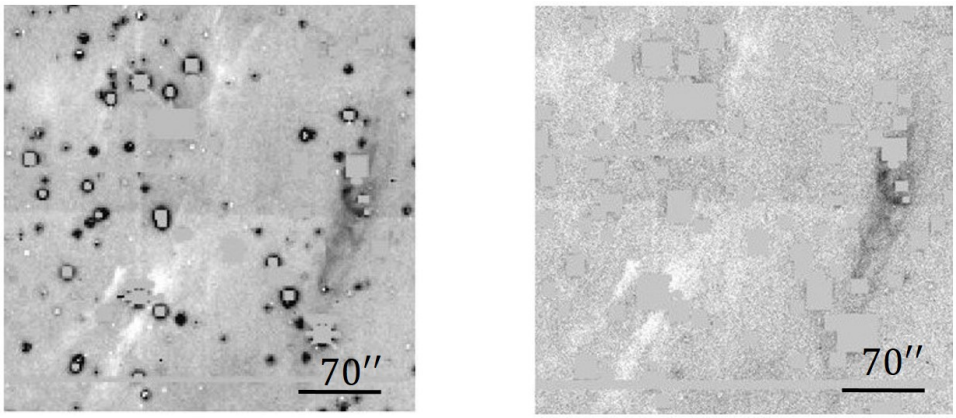

Figure 3.9: The LE#5 difference-image before and after the masking process as well as examining the appropriate pixel-value range for the left and right images, respectively.

3.2.5 LE#5

The first LE feature epoch in the LE#5 difference-image is the same as the first LE feature in the LE#4 difference-image, but between the two LE epochs in the LE#5

difference-image, there is a 3.95-year interval. The first epoch shows a trace of a filament in Figure 3.9.

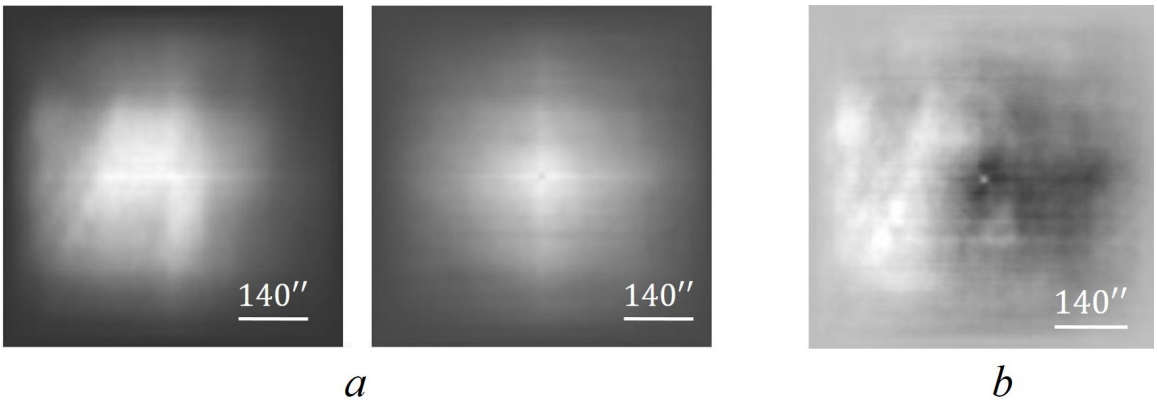

Figure 3.10: *a.* Left: The 2-D CC of the LE#5 region. Right: The 2-D CC of the control region. *b.* The net CC image which is the result of the subtraction of the two top images.

In contrast, the second epoch is divided into four features: one filament and one dust clump in the top-left half of the LE#5 difference-image and the other two in the bottom-left half with a divergence angle (see Figure 3.9). Hence, it is possible that every part of the second epoch does not relate to one echo depth with respect to the SNR of Cas A in our line of sight.

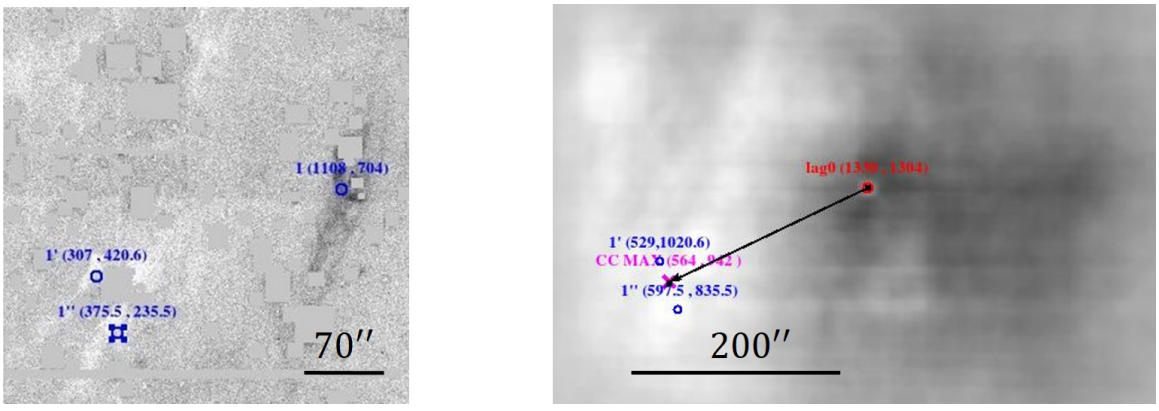

Figure 3.11: Bright points selected in both the LE#5 difference-image and the net CC image. The left panel also shows the LE CC and the lag 0 coordinates as magenta and red points, respectively.

Cross-correlation images for the LE and the control region difference-images are shown in Figure 3.10a on the left and right, respectively. Figure 3.10b shows the net CC image.

In Figure 3.11, the estimated maximum movement of the LE feature is shown with a black vector in the right panel and is compared with the chosen displacements in the left panel.

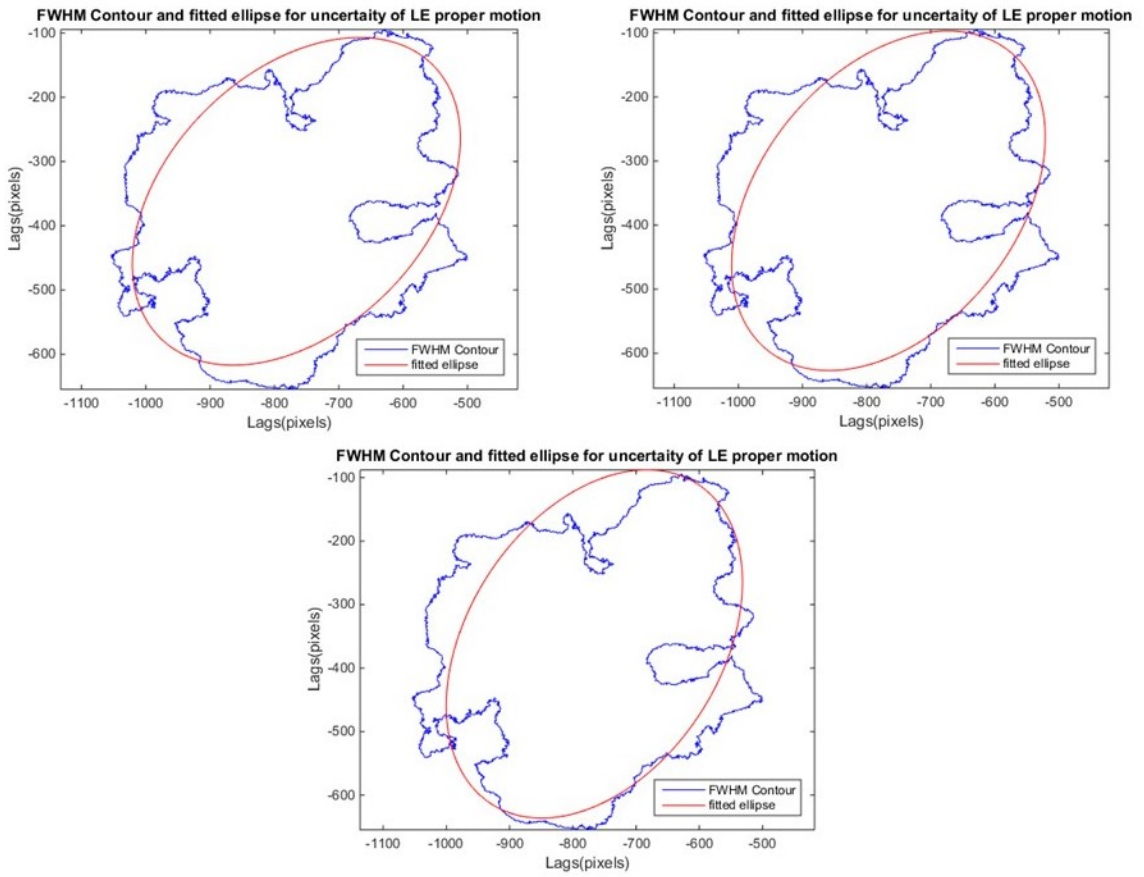

Figure 3.12: Fitted tilted ellipse with 45° (top left), 51° (top right), and 57° (bottom center) to the half-peak largest contour for the LE#5 CC.

Figure 3.12 from top left to middle bottom represents the estimated minimum, best-fit,

and maximum PA, respectively. In column 5 of Table 3.2 for LE#5, the PA is 231 ± 6 °. This is the direction in which the LE moves away from its SNR with respect to the north-east direction, while 45°, 51°, and 57° are the angles of the fitted ellipse to the half-peak largest contour of the LE CC.

Figure 3.13 indicates the same estimated minimum, best-fit, and maximum angle for the ellipse fit to the half-peak largest contour of the LE CC on the net CC image.

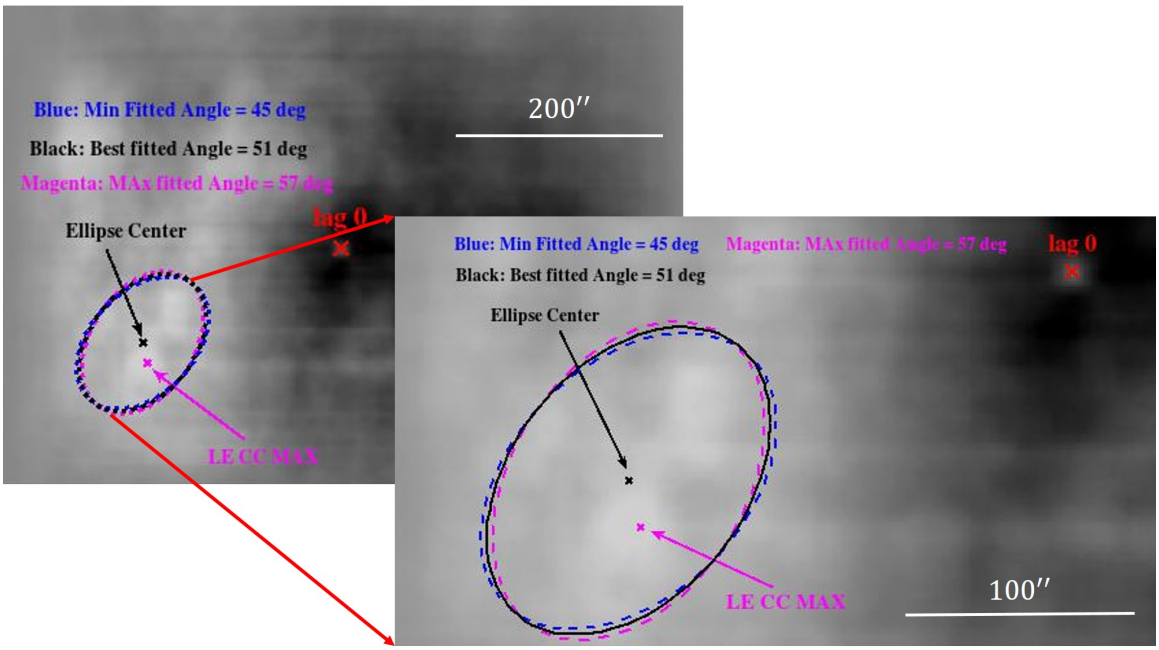

Figure 3.13: Fitted tilted ellipse to the LE#5 with 45°, 51°, and 57° as minimum, best-fit, and maximum angles, respectively.

There was a $\sim$ 20% relative uncertainty for the LE#5 APM magnitude and a 5% relative uncertainty for the LE#5 PA. The LE#5 APM magnitude was large and in the bottom of the lower range of its uncertainty, which is approximately consistent with the APM value of the expected echo depth in our line of sight (see Table 3.5). Two factors affected the magnitude and direction of the LE#5 APM when compared

to the previous case, LE#4. Comparing Figure 3.7 with Figure 3.9, LE#4 features look continuous in both epochs and had near-parallel shape while this factor did not apply for the LE#5 features. Also, the time difference for light features in the LE#4 difference-image was about two years, whilst the time gap for the LE#5 features was about twice that, or ~ 4 years.

3.3 Sample Light Echo Features Related to Tycho SN

In this section, for individual Tycho LEs, (LE#6 to LE#10), the LE features's characteristics and the result of the probable LE APM vectors are described in detail. All of the locations, the size of the selected sub-difference-images, and the pixel value ranges for both LE and control regions are shown in Table 3.10 for each Tycho probable LE difference-image.

Table 3.10: Location, image size, and pixel value ranges of Tycho LEs

LE number	LE Location w.r.t. Tycho	Possible related LE region image size	LE region pixel value range	Control region pixel value range
LE#6	south west	1700×620	-50 — +65	-40 — +40
LE#7	south west	784×928	-40 — +35	-35 — +32
LE#8	roughly south	850×310	-95 — +115	-40 — +40
LE#9	south east	980×580	-45 — +55	-45 — +55
LE#10	south east	1322×1156	-50 — +50	-50 — +50

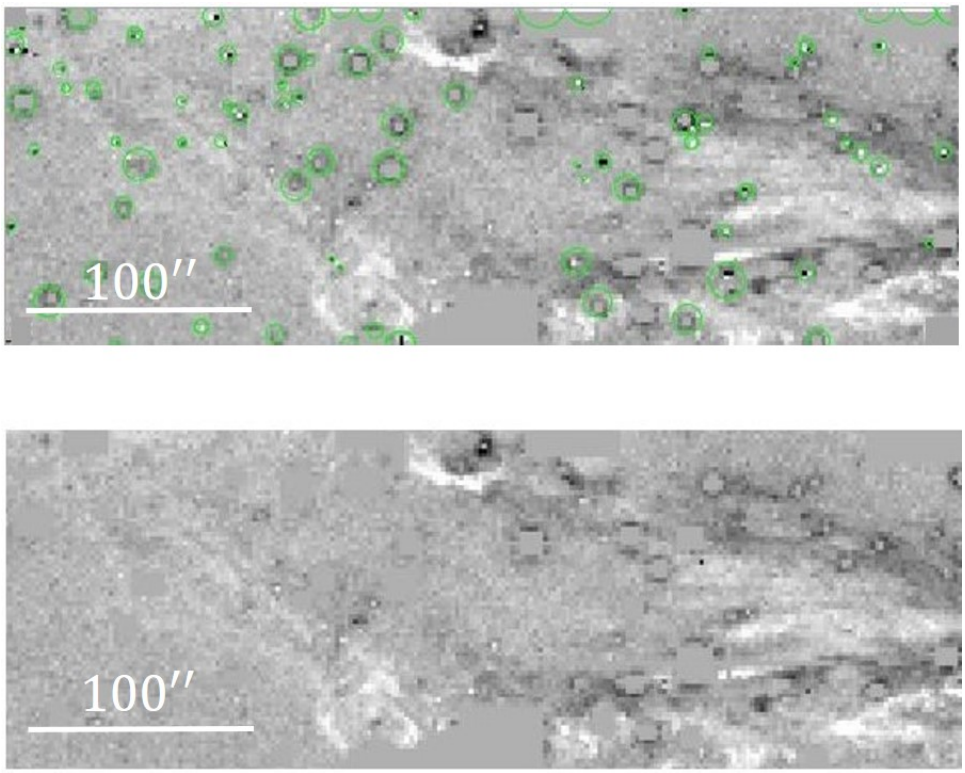

Figure 3.14: Top: The green areas have dead pixels or saturation for masking on the L E#6 image. Bottom: The LE#6 difference-image after the masking process.

3.3.1 LE#6

LE#6 does not have a simple figure. The LE#6 difference-image in Figure 3.14 shows that the LE features in the first epoch located in two different directions: (a) from the middle-right to top-center and (b) from the middle-right to bottom-center of the difference-image. It seems that the latter changed its direction from the bottom-center to middle-left of the difference-image. The same was true for the LE feature in the second epoch. So, the uncertainty in the LE net CC image should be high. It can be seen from Table 3.2 for LE#6 that the APM magnitude had a $\sim 59\%$ relative uncertainty and the position angle had a $\sim 9\%$ relative uncertainty.

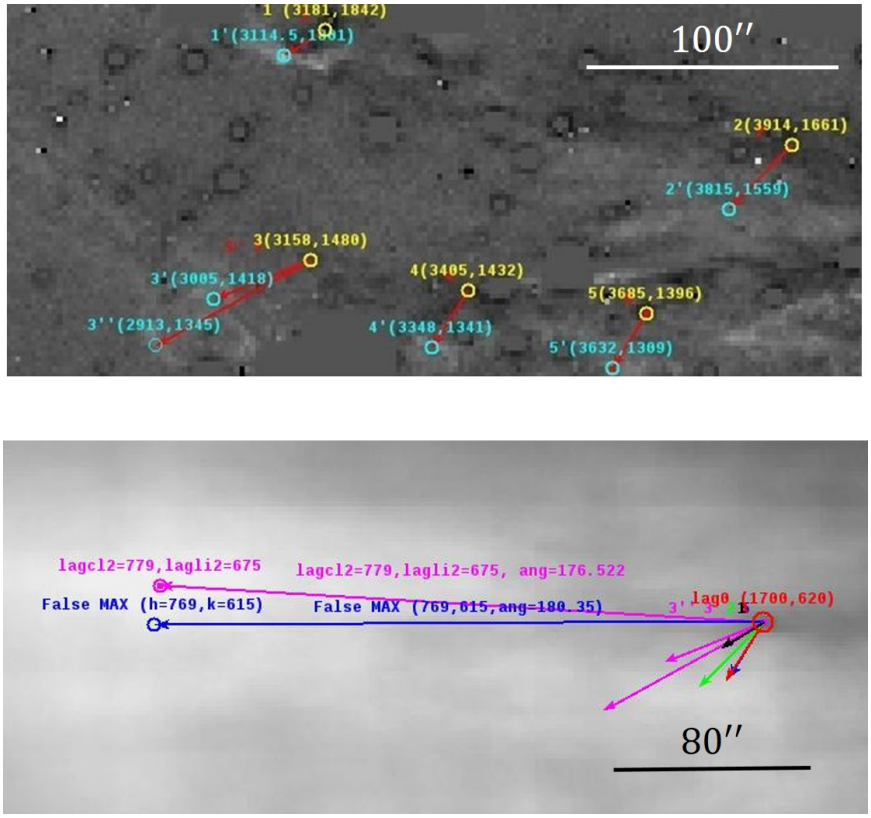

Figure 3.15: Top: Chosen vector motions for LE#6. Bottom: In the magnified net CC image of LE#6, the position of lag 0, coordinates of false maximum lags, and false LE CC are shown. Vector motions with respect to lag 0 are shown by black, green, and magenta (for small vector motions); blue (for small vector motions); and red as numbers 1, 2, 3′ and 3″, 4, 5 motion vectors, respectively. Note that motion vector numbers 4 and 5 are both in the same direction and of roughly equal length.

Figure 3.16 shows the net CC image (top left) and the zoomed-in region where ellipses were fitted to the largest contour of the half-peak (middle right) to show minimum, best fit, and maximum angles in degree as an acceptable direction range for the LE#6 PA. The bottom panel in Figure 3.16 also indicates the largest contour of the half-peak of the LE#6 2-D CC process as well as its best-fit ellipse. It is anticipated that this LE would be located in behind the source event at $-43.41pc$ (see Table 3.6). Although the uncertainty of the APM magnitude for this LE was very large, it was consistent with the expected APM at the mentioned echo depth, within 1σ. The PA for this LE

was obtained $(162.5 \pm 7.5)°$. This value does not have an agreement with the expected PA (188°) with respect to the LE midway and its SNR (see Table 3.2). Again, LE#6 has two main issues. As with LE#1, LE#6 does not have simple near-parallel LE features, and each epoch has more than one feature.

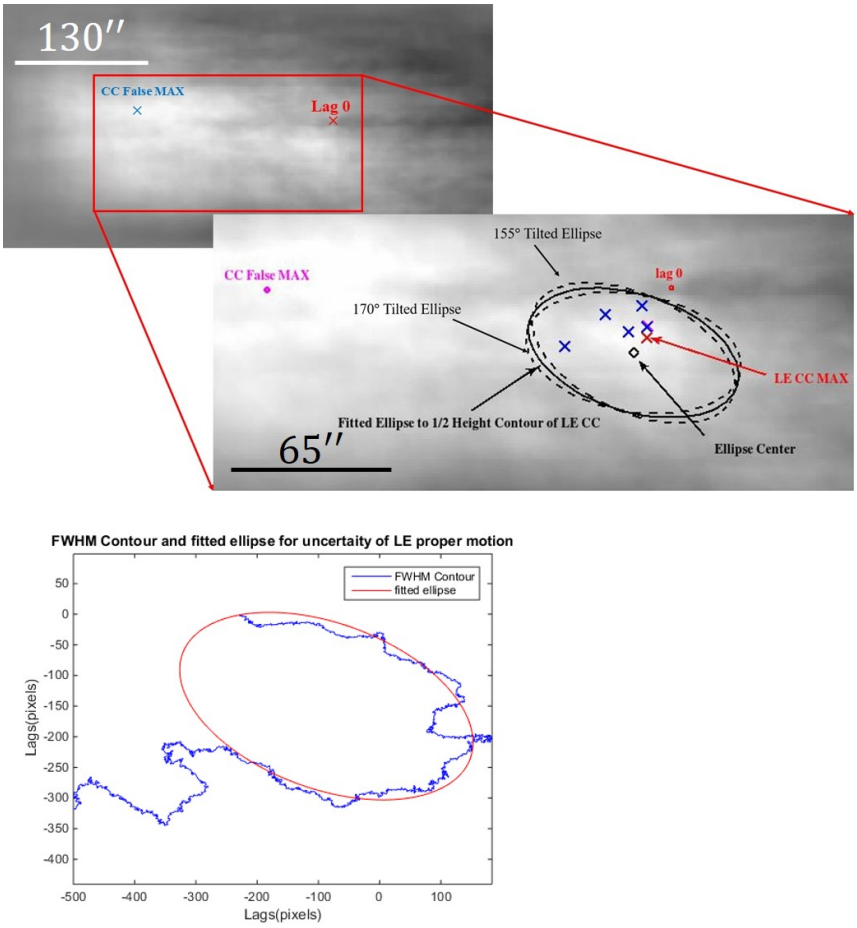

Figure 3.16: Top: Net CC image of LE#6. Middle right: The red box magnified to show minimum, best fit, and maximum angles of the fitted ellipse to the 2-D CC largest contour to get an appropriate direction as a position angle for the LE#6 CC. The blue crosses show the location of motion vectors 1-5. The LE CC is represented by the red cross and the best-fit ellipse center is marked by a black diamond. Bottom: Best-fit ellipse with 162.5° to the largest contour at the half-peak for the LE#6 2-D CC process.

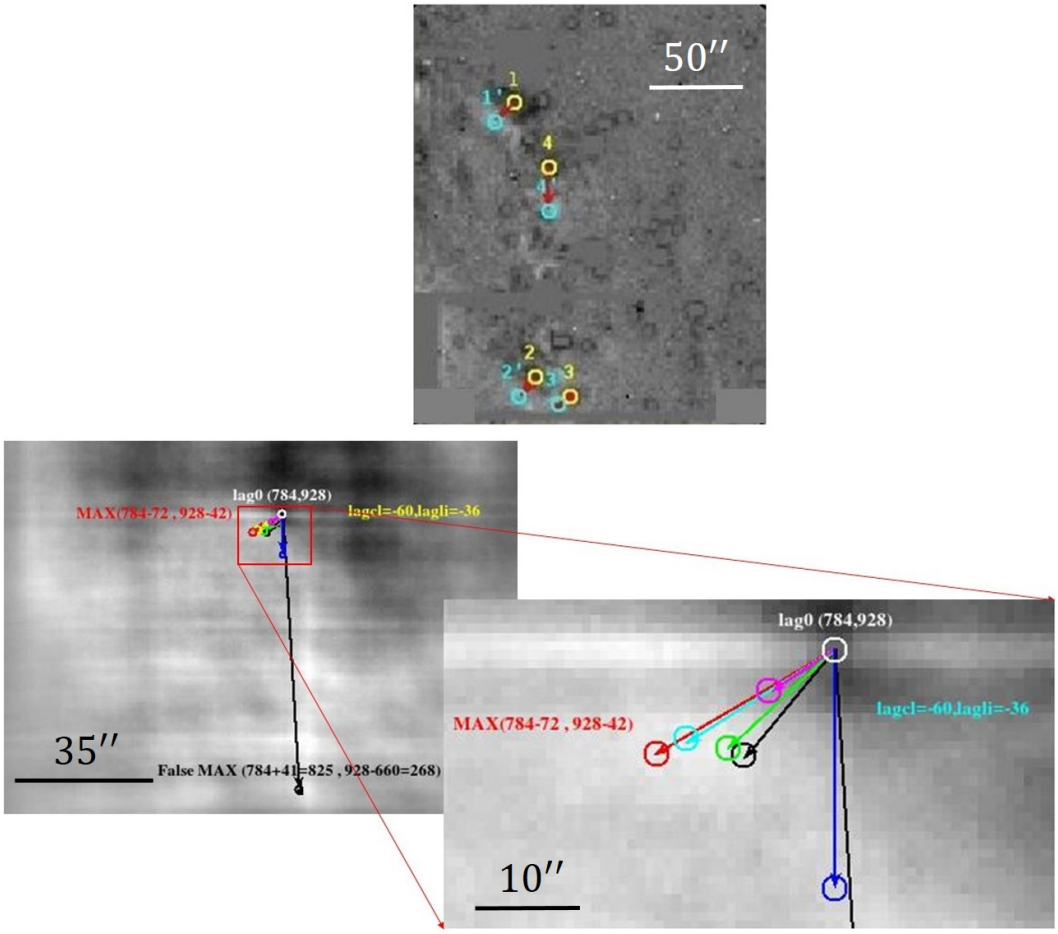

Figure 3.17: Top: Yellow and cyan circles show the bright points in the first and second LE#7 epochs, respectively. Small red vectors show the motion of points from the first to second LE#7 epochs. Bottom: The net CC image of LE#7 is shown. Also, the region of the LE#7 2-D CC (red vector), the best-fit ellipse center coordinates (cyan vector), and selected motion vectors (magenta, green, blue, and black vectors) are magnified of the figure.

3.3.2 LE#7

LE#7 is another LE located near LE#6. From Figure 3.17, it is evident that the motion vectors were very small during the $\sim 2yr$ interval. Therefore, it is expected that LEs are located behind the plane of the source event plane which we know from their z value.

Table 3.10 shows that the pixel value ranges for the LE and control regions are very close but not the same. This sample shows that if the pixel value ranges for both LE and control regions are taken equally, then the LE CC will be located in the negative contours of the CC values due to the subtraction between the two LE and control region CC images.

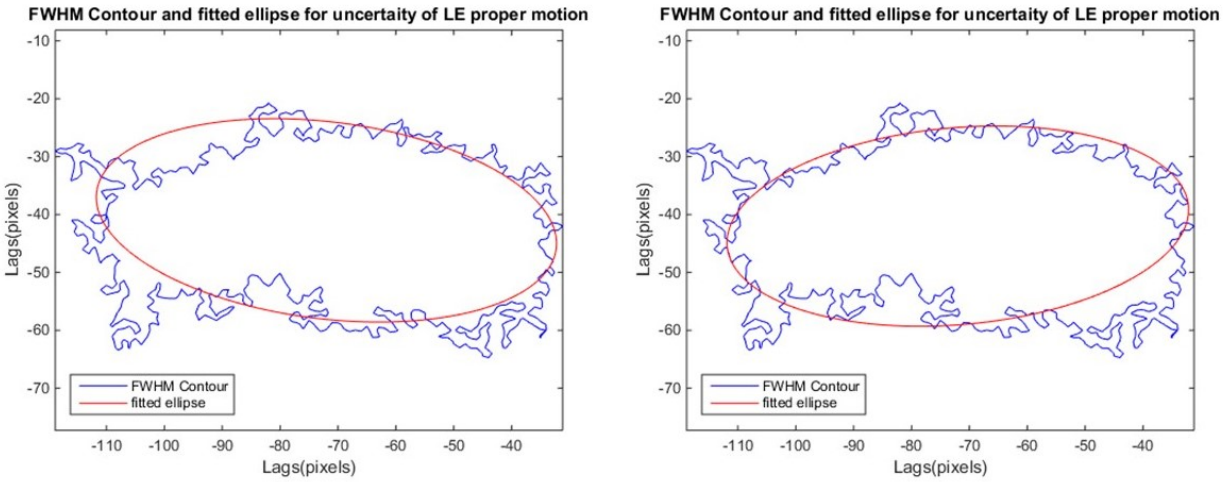

Figure 3.18: Best-fit ellipse to the half-peak largest contour of LE#7 2-D CC process with 175° (left) and 5° (right).

Table 3.2 indicates that the APM value has an 18% relative uncertainty and the PA has a $\sim 6\%$ relative uncertainty. However, when we obtained the expected echo depth for this LE with respect to the SNR plane, we found that LE#7 is behind the SNR plane ($z = -42.21pc$). The obtained result ($(11.2 \pm 2.0)\ ''yr^{-1}$) is far from the APM magnitude ($30.5\ ''yr^{-1}$) result for the expected z. To solve this discrepancy, we considered the possibility of the dust inclination (α) which would have to be $\alpha = 46.4°$ to explain the APM (see Table 3.6).

It should be noted that the best-fit ellipse for this LE can be set with angles between 175° and 185°. It is possible to also set the best-fit ellipse from 2° to 7° to the largest contour at the half-peak (see Figure 3.18). But, if we consider the location of

the best-fit ellipse with respect to lag 0, then it is obvious that the direction of the movement presents the correct value range for the PA to be between 175° and 185°. What we found as a result for the PA is almost consistent with the LE#7 PA value with respect to the mid-point between the LE features and the SNR, Tycho.

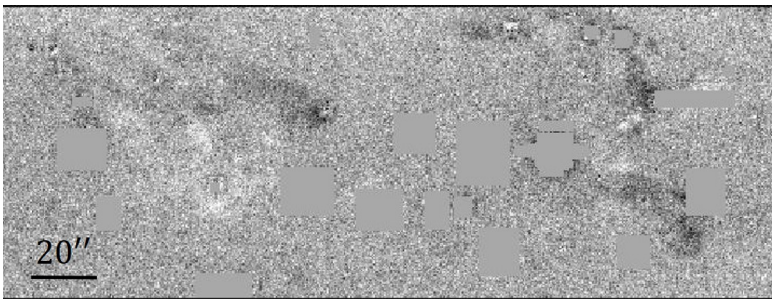

Figure 3.19: Difference-image of LE#8 with intense masking.

3.3.3 LE#8

LE#8 is one of the most complicated difference-images (see Figure 3.19). There are some dust clumps in the two epochs that are neither near parallel nor stripes in shape.

Table 3.2 shows that the APM magnitude has a 14% relative uncertainty and the position angle has a 6% relative uncertainty. The maximum value of the obtained PA is in agreement with PA from column 6 of Table 3.2 for LE#8. But, the APM magnitude range is inconsistent with the range predicted by Rest et al. (2008). Also, the expected echo depth (in front of the source plane) for this LE gives the APM magnitude as more than two times greater than the result we obtained. Again, suggest that dust inclination ($\alpha = 58.7°$) could resolve this discrepancy (see Table 3.6).

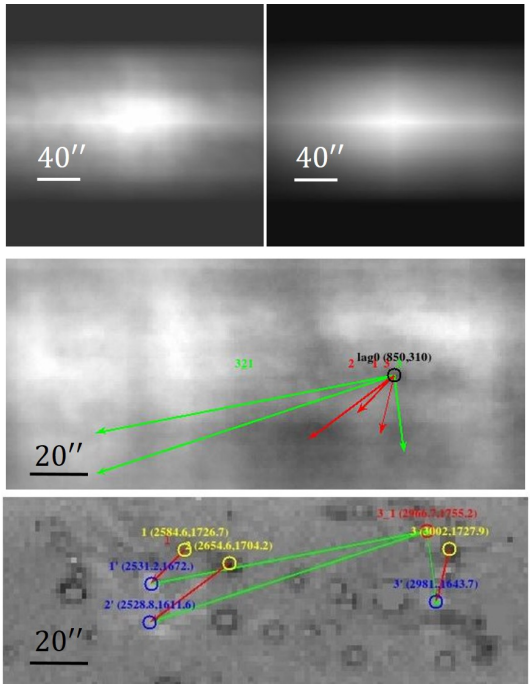

Figure 3.20: Top left: CC of LE#8 region sub-difference-images. Top right: CC of control region sub-difference-images. Middle: The net CC image result from the subtraction of the two above images with picked motion vectors shown as brighter points moving between the first and second LE epochs with respect to lag 0. Bottom: LE#8 difference-image with selected motion vectors. Brighter points represent movement between the first and second epochs.

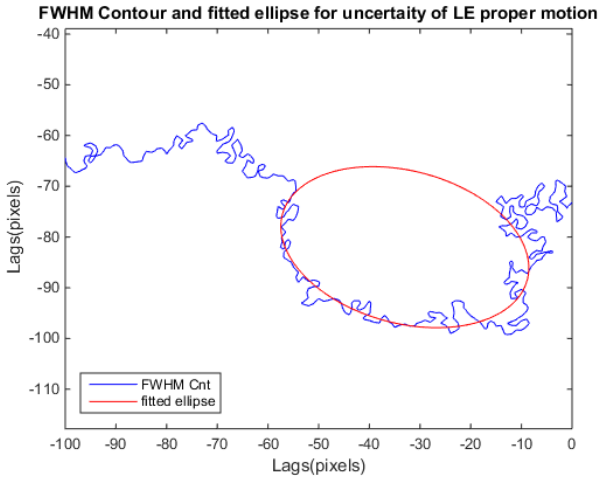

Figure 3.21: Best-fit ellipse to the half-peak largest contour of the LE#8 2-D CC.

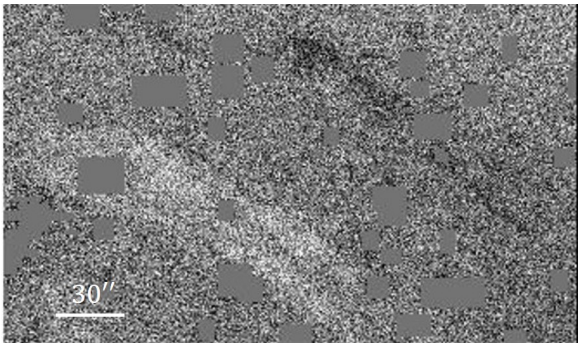

Figure 3.22: Difference-image of LE#9 with intense masking.

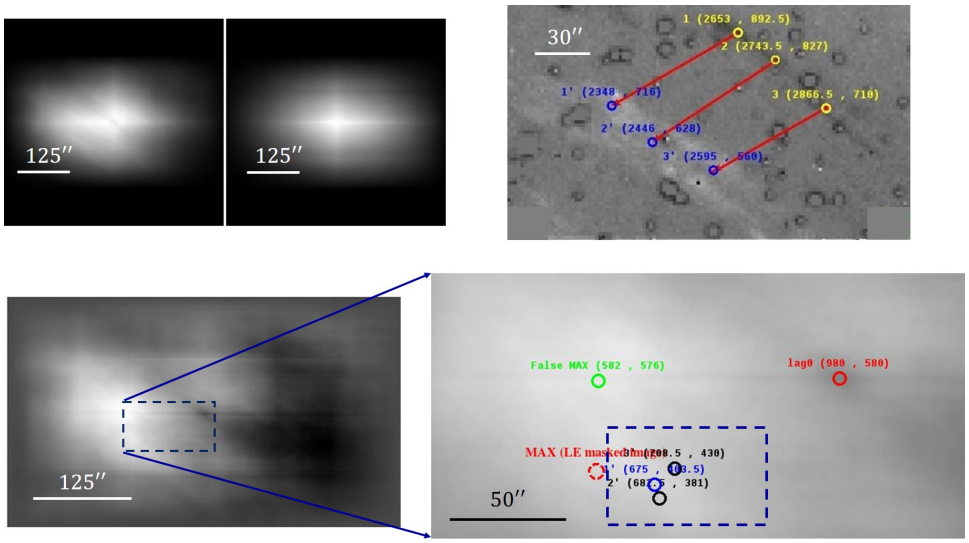

Figure 3.23: Top left: The 2-D CC of the LE#9 region and control region sub-difference-images, respctively. Top right: Yellow and blue circles show the brighter points in the first and second LE#9 epochs, respectively. Red vectors indicate the probable motion of points between two LE#9 epochs. Bottom left: The net CC image of LE#9. The dashed blue rectangle demonstrates that the region covers all the motion vector end points and also the LE 2-D CC location. The rectangle and its area are magnified in the right panel. Bottom right: The selected zoomed-in area of the left panel shows the position of lag 0 (red circle), vector motion end points w.r.t. lag 0 (black and blue circles), coordinates of false maximum lag before using the mentioned corrections (green circle), and the correct LE CC (dashed red circle).

3.3.4 LE#9

As Figure 3.22 makes clear, the LE#9's features look like two parallel stripes in which the first epoch is thin and the second epoch is wide and extended. In the bottom of the feature it seems that there are two parallel filaments which connected to each other later in the middle of the second epoch. So, there is the probability that the second epoch filaments are related to two different echo depths. Since the LE#9 features are near parallel, two approaches were chosen to identify the influence of the masking process on the result of the 2-D CC maximum. We performed the masking procedure on: (a) the LE region and (b) both the control region and the LE region.

Figure 3.22 illustrates the area of the LE#9 features where the intense masking process was performed based on the first approach. It can be seen from the Table 3.2 that the APM magnitude is $(38.6 \pm 8.2)\ ''yr^{-1}$ and PA is $(339 \pm 5)^{\circ}$ for LE#9. Therefore, the relative uncertainty for these values are 21% and 3%, respectively.

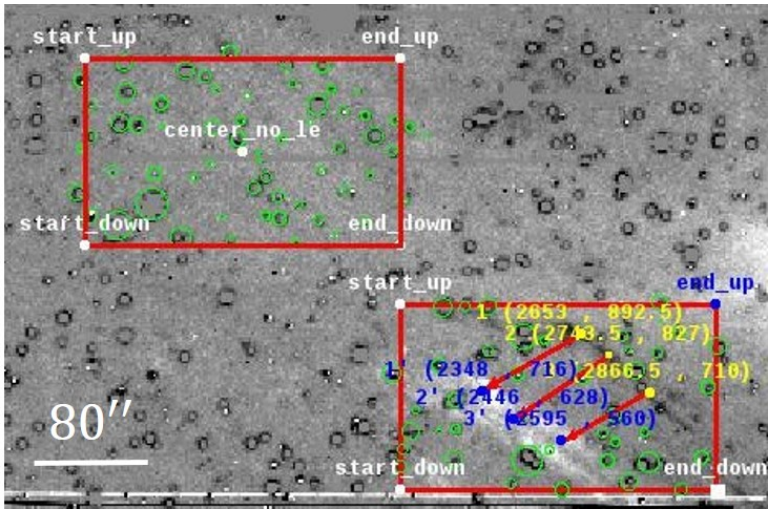

Figure 3.24: Image shows chosen difference-images with LE#9 features and also without them. Green circles are regions that needed intense masking.

In the second approach, in addition to the previously performed tasks, the masking process was also performed on the control region (see Figure 3.24). The result is noticeable. The APM magnitude and PA are $(38.0 \pm 9.1)\ ''yr^{-1}$ and 343°, respectively. The relative uncertainty for APM magnitude is 24%. The PA magnitude is in the range that is obtained in the former approach; i.e., $(339 \pm 5)°$.

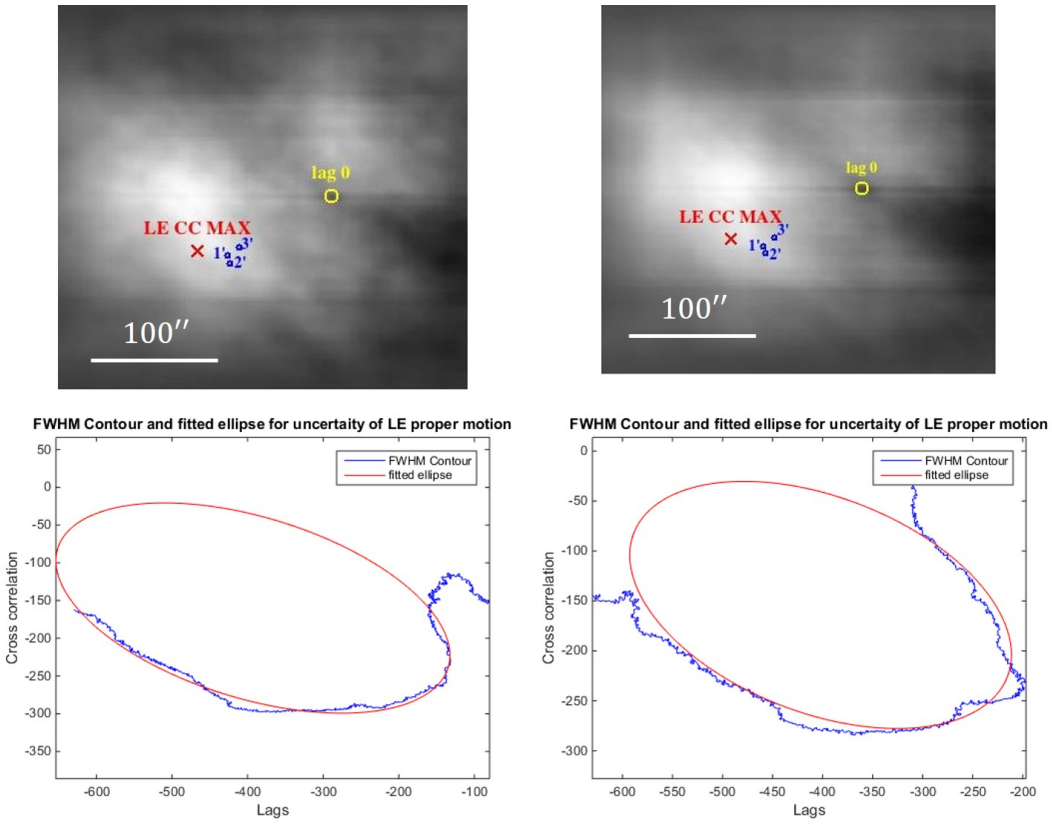

Figure 3.25: Top left: Magnified net CC image for LE#9 when both LE and control regions have had intense masking. Top right: When only the LE#9 region difference-image has had intense masking. Both top images show coordinates of lag 0, brighter points in the second epoch of LE#9 difference-image, and the LE CC value. Bottom left: The best-fit ellipse (tilt angle = 343°) to the half-peak largest contour of the LE#9 2-D CC when both sub-difference-images have had intense masking. Bottom right: The best-fit ellipse (tilt angle = 339°) to the half-height contour of the LE#9 2-D CC contour when only the LE#9 sub-difference-image has had intense masking.

Figure 3.25 presents the net CC images for both mentioned approaches (top). Also, it displays the largest contours at the half-peak and their best-fit ellipses in both cases, with angles equal to 343° and 339°, respectively (see the bottom panel of Figure 3.25). Comparing these two recent cases reveals that performing the masking process on the control region does not have a remarkable influence on the final obtained result.

3.3.5 LE#10

The LE#10 image was observed in the neighbourhood of LE#9. It can be seen from Figure 3.26 that the LE#10 features are in a near-parallel stripe shape and are very close to each other.

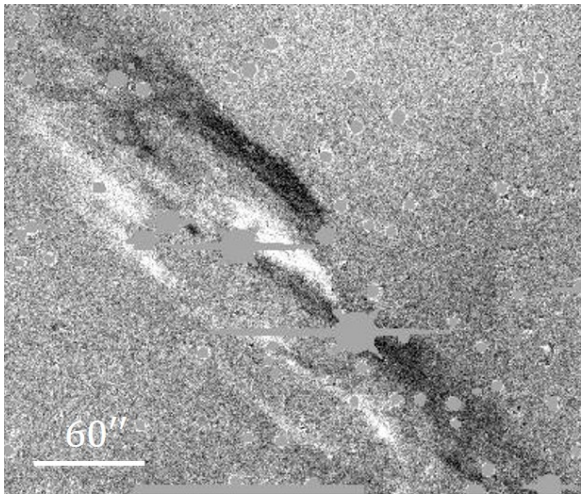

Figure 3.26: Difference-image of LE#10 with intense masking.

In the top-left and bottom-left panels of Figure 3.27, the potential region of obtaining LE CC is indicated by a red tilted ellipse.

The APM magnitude with its standard deviation is $(33.7 \pm 7.6)''yr^{-1}$ with about a 23% relative uncertainty, and the PA is $141° \pm 2°$ which shows very low relative uncertainty $\sim 1\%$. Both APM magnitude and PA are in a good agreement with previous research reported by Rest et al. (2008) where the LE#10 PA was reported as $135.5° \pm 17.1°$ (Rest et al., 2008; Rest, Foley, et al., 2011).

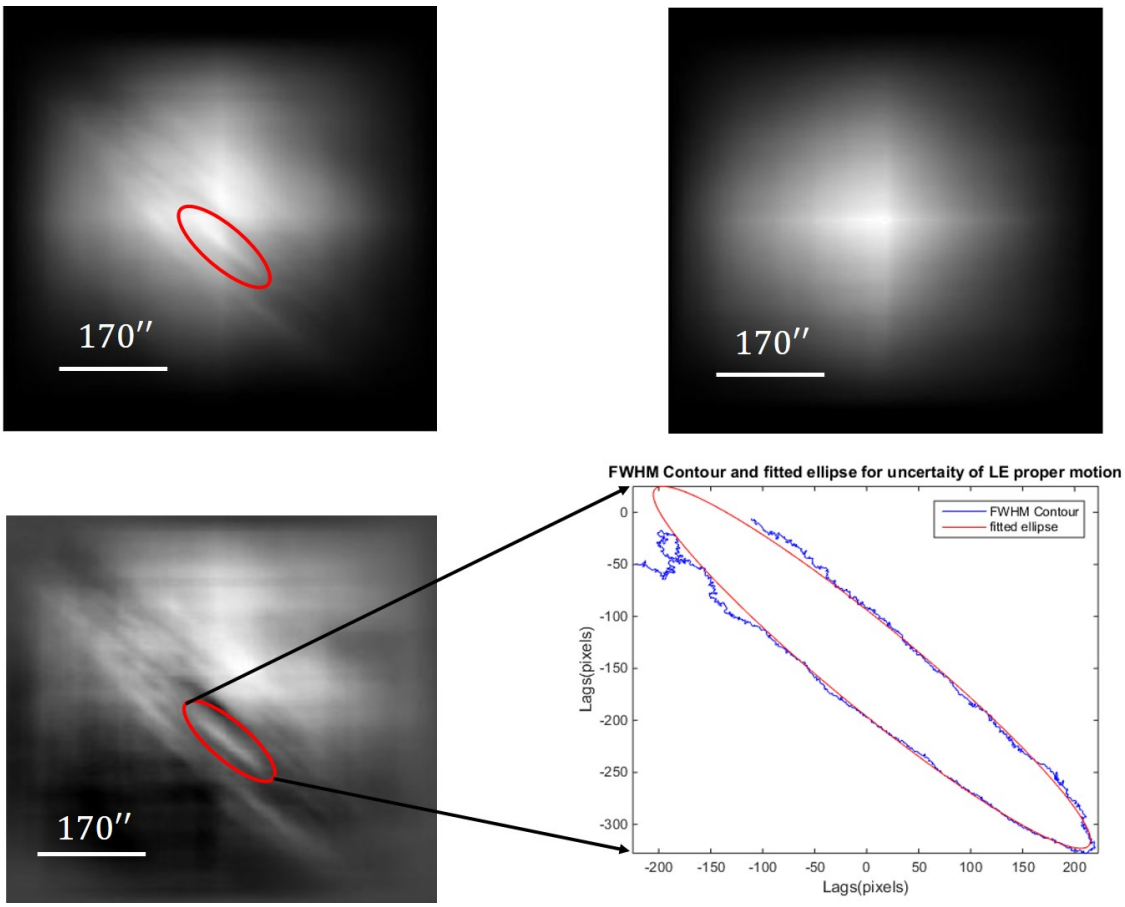

Figure 3.27: Top left: The 2-D CC of LE #10 region. The red tilted ellipse indicates the potential region of obtaining the LE CC maximum and best-fit ellipse. Top right: The 2-D CC of the control region. Bottom left: The net CC image of LE#10. Bottom right: The best-fit ellipse with 141° to the largest contour at the FWHM of LE#10 is found in the region of the red tilted ellipse shown in the bottom-left panel.

LE#10 is the only case which demonstrated good agreement between this study and the previous one reported by Rest et al. (2008). The interval ($\Delta t = 1.15\ yr$) between the two epochs was the minimum among all the studied samples. Additionally, the existence of the near-parallel stripe-shaped LE features, is another possible reason for the consistency in results, however, the first and second LE epochs are not uniform and there are disconnections between the features for each epoch. If we assume that the LE features are not related to one echo depth, then it can be concluded that when the time interval is not more 420 days and the LE features are in near-parallel stripe shape, the average of the different APM magnitudes relevant to different echo depths is more reliable within 1σ uncertainty compared to longer intervals and non-parallel stripe shapes. However, there is a bit of discrepancy between the obtained LE PA from this method and the PA value from the mid-point between the LE features with respect to the SNR, Tycho.

Chapter 4

Discussion

We have examined apparent LEs in ten difference-images. All twenty astronomical images used to form the difference-images were taken at the KPNO 4-meter Mayall telescope using the wide FOV CCD Mosaic-1.1 imager (Schweiker et al., 2011). Each of the ten difference-images were prepared by using the Pan-STARRS pipeline.

4.1 Characteristics of the Probable LE Samples

Among our difference-image samples, we have different time intervals, various LE features, and different number of LE features for each epoch. In the following, the effect of each of these factors is discussed.

1. **Time interval**

   The probable LE samples are categorized into four groups. We have samples with 1.15, 1.93, 2.25, 2.9, and 3.95 yr intervals. Except for the 1.93 interval, we have one sample from each. Having a long time interval leads the dust concentration varying more with location. So, the measurement is less local and

the scattered dust is not uniform. By evaluating the results, the following cases can be discussed.

1.1) *A difference-image with the same grid of the sky and time interval*: The results of our study of LE#4 is in agreement with the previous study reported by Rest et al. (2011). In our study, the obtained APM magnitude within 1σ covers the APM magnitude expected for $z = 629.12$ pc (see Table 3.5). Compared to Rest et al.'s (2011) result (65°), our studied case PA direction result (71.5°) is 8.5% closer to the PA direction calculated with respect to the mid-point between the LE features and their related SNR coordinates (77°).

1.2) *Difference-images with the same grid of the sky and different time intervals*: First, Rest et al.'s (2011) PA direction result (299.1° with an 80-day interval) for LE#1 indicates that LE#1's PA was 31.75% closer to the PA direction calculated than our obtained result (199° with a 2.25-year interval) with respect to the mid-point between the LE features and their related SNR coordinates (see Figure **??**). Second, compared to the LE#5 PA direction result (51° with a 3.95-year interval), LE#4's PA direction result (71.5° with a 1.93-year interval) indicates that it is 26.6% closer to the PA direction calculated with respect to the mid-point between the LE features and their related SNR coordinates (77.3°) (see Table 3.2). Additionally, the LE#4 APM magnitude result (46.3 $''yr^{-1}$) is 21.5% closer to the APM magnitude expected for the $z \simeq 630$ pc than LE#5's (56 $''yr^{-1}$). In the case of both LE#1 and LE#4, the shorter interval results in a more accurate estimate of the true PA direction. This means that in both pairs of cases a longer difference time of observations negatively affects the estimation of PA direction (see Table 3.2: compare the values of columns 5 and 7 with column 6 for LE#1 as well as the value of column 5 with column 6 for LE#4 and LE#5).

1.3) *Difference-images with different grid of the sky and time intervals*: The LE#10 (with a 1.15 yr interval) has the smallest time gap among the samples

studied. This sample is one of the common cases, with a previous study reported by Rest et al. (2008). Both the APM magnitude and PA value from this study are in a good agreement with theirs (see Table 3.2). Also, this sample shows the best goodness of fit amongst the samples studied in contrast to LE#5 (with a 3.95 yr interval), which has the longest time difference.

All of the cases studied here and some the cases discussed in some previous works (Rest et al., 2008; Rest, Foley, et al., 2011) indicate that the optimum time interval for finding accurate results is from three months to one year. An interval less than 3 months in length leads to LE features covering each other so that they are not distinguishable from each other. On the other hand, an interval longer than one year leads to a decrease in the illuminated scattered dust due to its uniformity of structure and an increase in the relative uncertainty the of APM magnitude and PA direction estimations.

2. **LE feature shapes**

   The second factor influencing the estimation of the APM vector is the shapes of the LE features. As I explained in Chapter 1, it is considered that LE features located in dust filaments. If they intercept the LE ellipse and are bright enough, then there can be an expectation of observing them. Amongst the samples investigated with a 1.93 yr interval, the samples which have two near-parallel and striped shape LE features (e.g., LE#4) have the best results and also the best goodness of fit (see the LE#4, the LE#8, and the LE#6 and compare the LE#4 with the two latter cases). Additionally, having equal size, thickness, and extended shapes assist in better understanding dust filaments and interstellar environment and in obtaining a more accurate LE APM vector estimation (see the LE#4 and the LE#3 and compare them with each other). In some cases (e.g., LE#9), it can be seen that having factors of equal size, thickness, and extended shapes covers the negative effect of the long interval (2.9 yr) in comparison with

shorter time intervals, such as the 1.93 interval cases and 2.25 interval, and these factors contribute to better and more accurate results and goodness of fit.

3. **Number of LE features**

   For one LE feature in each epoch, the average of the APM vector of the LE feature was found which indicates that the obtained magnitude and direction are average values for the whole LE feature in that epoch. However, a greater number of LE features has both advantages and disadvantages. The advantage of having more than one feature in each epoch is the increase in the precision of the calculated APM vector. On the other hand, when there is more than one LE feature for each epoch, there is an ambiguity in calculating the APM vector. In this case, two probable scenarios are possible: (a) the obtained APM vector may indicate the average of the APM vectors from different projected echo depths, or (b) the obtained APM vector is from the average of the LE features related to one echo depth. Also, this issue leads to the elevation of the uncertainty of the PA direction such as the case of LE#10. This LE has the best goodness of fit; however, its PA is slightly higher than the PA with respect to the mid-point between the LE features and their source event (Tycho).

4.2 Issues Involved in the 2-D CC Method

During our study, some common drawbacks among all the samples were identified. In the following, three common issues will be explained.

1. **Residuals**

   Although the Pan-STARRS pipeline was used to produce the difference-images, there were still some residuals in the difference-images, such as small white and black areas which are probably the remains of cosmic rays or dead pixels. Hence,

the masking process and, in some cases, even an intensive one, was needed to improve the result of APM magnitude error from 2σ to 1σ.

2. **Dependent method**

   In the 2-D CC method, the entirety of the LE features are considered as one system. This approach is more of an overall approach, taking care of all LE features in one step. In contrast, the previous approach (Rest et al., 2008; Rest, Foley, et al., 2011) was based on visually measuring the APM vector arclet by arclet. In the current approach, pixel value has significant effect. In most cases studied, the the pixel-value range of the control region is very close to the LE region's, which leads the LE CC to not be the maximum of the 2-D net CC. Therefore, we need to visually consider some probable displacement vectors on the LE difference-images like the previous study reported by Rest et al. (2008) to find the correct LE CC.

3. **Underestimated uncertainty**

   If the negative effect of the residuals and control region is considerable, then it can lead to the existence of some peaks which do not relate to the LE CC. Hence, eliminating the irrelevant peak from the LE CC peak results in a smaller and underestimated standard deviation due to the smaller obtained half-peak intensity level. This issue happened for LE#4.

Chapter 5

Conclusions and Future Work

5.1 Conclusions

The aim of this thesis was to characterize a new method to determine the LE APM vector and to test its usefulness compared to the "visual "approach.

In Chapter 2, we clearly described our new computational method in determining the LE APM. We explained how to run the CC technique as an implementation of the Fourier Transform. Moreover, an explanation of distinguishing features observed in the CC of a pair of difference-images of LE features was given in Section 2.5.

In Section 2.6, all the stages taken to get the LE APM vector were fully mapped out. Then, the investigation of the LE CC was described in three steps. Here it was mentioned that using only this computational method is not sufficient. Thus, the previous visual measuring method is also needed to confirm that the LE APM magnitude as well as PA direction are correct. In section 2.7.4, I reviewed and completed the explanation of how we obtained the uncertainty of the APM vectors. Also, the methods used to establish goodness of fit were described in Section 3.1.1.

The R–squared, RMSD, and NRMSD were applied to find the goodness of fit for LE samples. Because the half-peak largest contour of the LE feature motions are various, I concluded that to get the reliable fit, all three of the methods described in this thesis must be applied. The goodness of fit for the Cas A and Tycho LEs' APM are illustrated in the Table 3.7 and Table 3.8, respectively.

In section 3.3.4, I showed that performing the masking process on the control region in addition to the LE region does not have a noticeable influence on the net CC image result.

As I discussed in the Section 4.1, time interval, LE features, and the number of LE features have critical roles in the estimation of APM vectors by using the introduced method. I deduced that the optimum time interval between two observation times is from about three months to one year. Because an interval less than 3 months in length leads to the possibility that LE features would not be distinguishable. In addition, by increasing the time interval the uniformity of dust is declining and it leads to have dust with different compactness and thickness.

The number of existent LE features in each epoch is the other factor that tends to reduce the expected precision of the APM vector estimation. This means that,it is not obvious whether an obtained APM vector is related to one echo depth or not. This debate is also open for more investigation. In Section 5.2, the debate surrounding the inclination of the dust filaments was discussed.

While the PA direction of LEs was the most important quantity in the previous studies of Rest et al. (2008) and (2011), we are the first to introduce a method to obtain the LE APM vector estimation as well as the LE APM uncertainty. Taking all factors mentioned into account, the current study shows that the obtained results are in good agreement with previous research reported by Rest et al. in 2008 and 2011. The results also show: (a) a good agreement within 1σ with the APM magnitude for the expected

echo depth, z, as well as (b) a consistency within 2σ with PA calculated with respect to mid-point between the LE features and their relative SNR coordinates, in most cases. In addition, for the expected echo depth, z, the range of probable inclinations for dust filaments corresponding to the range of estimated APM for each LE sample was found. All ten samples showed acceptable results; however, the result is more accurate (i.e., there is less uncertainty as well as a smaller bias) when the time interval is about one year (at maximum) or when there is only one LE in each image. Finally, compared to the previous manual technique, there were much less manual measurements were taken for the whole LE features in one frame. Considering all the challenges, the CC method is favourable as the APM vector uncertainty can be determined, which has not been achievable with previous method before.

5.2 Future of the Apparent Proper Motion Study

There remain some unsolved questions in this study. Future works will clarify our understanding of the LE APM vector.

1. Our study started with working on the difference-images prepared with the use of the Pan-STARRS pipeline before we obtained them. The difference-images showed that there were lots of remaining residuals adjacent to the LE regions. In some cases, there were remaining PSF wings and this maybe related to the fact that the row images were taken at different times, possibly leading to different PSF wings in each observation. In most of the cases, the pipeline could not remove the saturations perfectly; also, there were lots of black and white small areas in the vicinity of the LE regions with pixel values comparable to the LE pixel values. In addition, since the Galactic source events are located close to the Galactic plane, recognizing a LE feature from scattered light is challenging due to optical reflections from bright stars. The shift in location of ghost pupils due to differences in telescope pointing can produce non-LE CC features.

If we fail to eliminate these areas then the result of the 2-D CC will contaminate with them and the standard deviation will increase. Thus, it is critical to improve the difference imaging process for the automated pipelines such as Pan-STARRS in order to improve the LE APM vectors' measurement.

2. Most of the difference-images contained more than one probable LE feature for each epoch.This can cause vagueness in identifying the APM vector of the LE feature located in the projection of the echo depth, z, in the line of sight. The existence of more than one LE feature leads to two scenarios. First, if the LE features are located at more than one echo depth, then the APM vector is the average of the different APM vectors, and it does not represent the average APM vector of the entirety of the one LE feature at one echo depth. Second, if all of the LE features in one epoch are related to one common echo depth, the precision of calculating the average APM vector increases due to the number of LE features in one epoch. Using multiple observation from the same grid of the sky (Sinnott, 2013) with epochs separated by at least three months can give a solution to these two scenarios.

3. Table 3.5 and Table 3.6 summarize the probable inclined dust filaments for the estimated APM magnitude in the plane of the sky with respect to the source event plane in addition to the case that we estimated the LE APM with zero inclination for the expected echo depth. Further studies can determine which case is more probable for the estimated echo depth. The apparent motion of LE can be monitored and the dust inclination can be determined by taking the advantage of multiple epochs (Sinnott et al., 2013; Sinnott, 2013). This means that having more than two epochs for each LE, increases the accuracy of dust inclination.

References

Ackermann, M., Ajello, M., Allafort, A., Baldini, L., Ballet, J., Barbiellini, G., ... Bellazzini, R. (2013). Detection of the characteristic pion-decay signature in supernova remnants. *Science*, *339*(6121), 807–811.

Alard, C. (2000, jun). Image subtraction using a space-varying kernel. *Astronomy and Astrophysics Supplement Series*, *144*(2), 363–370. doi: 10.1051/aas:2000214

Alard, C., & Lupton, R. H. (1998, aug). A Method for Optimal Image Subtraction. *The Astrophysical Journal*, *503*(1), 325–331. doi: 10.1086/305984

Albinson, J. S., Tuffs, R. J., Swinbank, E., & Gull, S. F. (1986). Neutral hydrogen towards 3C 10, the remnant of Tycho's supernova. *Monthly Notices of the Royal Astronomical Society*, *219*(2), 427–439.

Ashworth Jr, W. B. (1980). A probable flamsteed observations of the cassiopeia-a supernova. *Journal for the History of Astronomy*, *11*, 1.

Baade, W., & Zwicky, F. (1934). Cosmic rays from super-novae. *Proceedings of the National Academy of Sciences*, *20*(5), 259–263.

Bertin, E., Mellier, Y., Radovich, M., Missonnier, G., Didelon, P., & Morin, B. (2002). ASP Conf. Ser. Vol. 281, Astronomical Data Analysis Software and Systems XI.

Brown, R. H., & Hazard, C. (1952). Radio-Frequency Radiation from Tycho Brahe's Supernova (AD 1572).

Brown, R. H., & Hazard, C. (1953). A radio survey of the milky way in Cygnus, Cassiopeia and Perseus. *Monthly Notices of the Royal Astronomical Society*, *113*(2), 109–122.

Cappellaro, E., Patat, F., Mazzali, P. A., Benetti, S., Danziger, J. I., Pastorello, A., ... Turatto, M. (2001). Detection of a Light Echo from SN 1998BU. *The Astrophysical Journal*, *549*, L215–L218.

Cappellaro, E., & Turatto, M. (2001). Supernova types and rates. In *The influence of binaries on stellar population studies* (pp. 199–214). Springer.

Chevalier, R. A., Kirshner, R. P., & Raymond, J. C. (1980). The optical emission from a fast shock wave with application to supernova remnants. *The Astrophysical Journal*, *235*, 186–195.

Chromey, F. R. (2010). *To Measure the Sky An Introduction to Observational Astronomy.* New York, USA: Cambridge University Press.

Condon, J. J., & Ransom, S. M. (2010). *ESSENTIAL RADIO ASTRONOMY.* Retrieved from `http://www.cv.nrao.edu/course/astr534/FourierTransforms.html`

Couderc, P. (1939). Les auréoles lumineuses des novae. In *Annales d'astrophysique* (Vol. 2, p. 271).

Crotts, A. (1988). Supernova 1987A in the Large Magellanic Cloud. *International Astronomical Union Circular*, *4561*, 4.

Crotts, A. P. S. (1988). Discovery of optical echoes from supernova 1987A-new probes of the Large Magellanic Cloud. *The Astrophysical Journal*, *333*, L51–L54.

Fesen, R. A., Hammell, M. C., Morse, J., Chevalier, R. A., Borkowski, K. J., Dopita, M. A., ... van den Bergh, S. (2006). The expansion asymmetry and age of the Cassiopeia A supernova remnant. *The Astrophysical Journal*, *645*(1), 283.

Gaskell, C. M., Cappellaro, E., Dinerstein, H. L., Garnett, D. R., Harkness, R. P., & Wheeler, J. C. (1986). Type Ib supernovae 1983n and 1985f-Oxygen-rich late time spectra. *The Astrophysical Journal*, *306*, L77–L80.

Giacobbe, F. W. (2005). How a type II supernova explodes. *Electronic Journal of Theoretical Physics*, *2*(6), 30–38.

Green, D. A. (2002). Historical supernovae and their remnants. *Highlights of Astronomy*, *12*.

Green, D. A. (2014). *A Catalogue of Galactic Supernova Remnants.* Retrieved from `www.mrao.cam.ac.uk/surveys/snrs/snrs.info.html`

Hillebrandt, W., & Niemeyer, J. C. (2000, sep). Type Ia Supernova Explosion Models. *Annual Review of Astronomy and Astrophysics*, *38*(1), 191–230. doi: 10.1146/annurev.astro.38.1.191

Iben Jr, I., & Tutukov, A. V. (1984). Supernovae of type I as end products of the evolution of binaries with components of moderate initial mass (M not greater than about 9 solar masses). *The Astrophysical Journal Supplement Series*, *54*, 335–372.

Jannuzi, B. T., Claver, J., & Valdes, F. (2003). The NOAO Deep Wide-Field Survey MOSAIC Data Reductions.

Krause, O., Birkmann, S. M., Usuda, T., Hattori, T., Goto, M., Rieke, G. H., & Misselt, K. A. (2008). The Cassiopeia A supernova was of type IIb. *Science*, *320*(5880), 1195–1197.

Krause, O., Tanaka, M., Usuda, T., Hattori, T., Goto, M., Birkmann, S., & Nomoto, K. (2008). Tycho Brahe's 1572 supernova as a standard Type Ia as revealed by its light-echo spectrum. *Nature*, *456*(7222), 617–619.

Lee, J.-J., Koo, B.-C., & Tatematsu, K. (2004). The environment of Tycho: Possible interaction with the molecular cloud. *The Astrophysical Journal Letters*, *605*(2), L113.

Liu, J.-F., Bregman, J. N., & Seitzer, P. (2003). A Scattered Light Echo around SN 1993J in M81. *The Astrophysical Journal*, *582*, 919–923.

McDonald, J. B. (2012). The Search for Supernova Light Echoes from the Core-Collapse Supernovae of AD 1054 (Crab) and AD 1181.

NASA, ESA, & the Hubble Heritage STScI/AURA-ESA/Hubble Collaboration. (n.d.). *Cassiopeia A - The colourful aftermath of a violent stellar death.* Retrieved from `http://www.spacetelescope.org/images/heic0609a/`

NASA/CXC/Rutgers/J.Warren & J.Hughes et al. (2005). *Tycho's Supernova Remnant: Tycho's Remnant Provides Shocking Evidence for Cosmic Rays.* Retrieved from `http://chandra.harvard.edu/photo/2005/tycho/`

NOAO. (2009). *Proposal Information for 2009A-0110.* Retrieved from `https://www.noao.edu/perl/abstract?2009A-0110`

NOAO. (2014). *KPNO Telescope Schedules Archive.* Retrieved from `https://www.noao.edu/kpno/forms/tel{_}sched/archive.html`

Osterbrock, D. E. (2001). Who Really Coined the Word Supernova? Who First Predicted Neutron Stars? In *Bulletin of the american astronomical society* (Vol. 33, p. 1330).

Pence, W. D. (2014). *A Primer on the FITS Data Format.* Retrieved from `http://fits.gsfc.nasa.gov/fits{_}primer.html`

Rest, A., Becker, A. C., Bergmann, M., Blondin, S., Challis, P., Clocchiatti, A., ... Huber, M. E. (2007). Light Echoes from the Historical Galactic Supernovae Cas A and Tycho. In *Bulletin of the american astronomical society* (Vol. 39, p. 935).

Rest, A., Foley, R., Sinnott, B., Welch, D., Badenes, C., Filippenko, A., ... Suntzeff, N. (2011, may). Direct Confirmation of the Asymmetry of the Cas A Supernova with Light Echoes. *apj*, *732*, 3.

Rest, A., Sinnott, B., & Welch, D. L. (2012). Light Echoes of Transients and Variables in the Local Universe. *Publications of the Astronomical Society of Australia*, *29*(4), 466–481.

Rest, A., Sinnott, B., Welch, D. L., Foley, R. J., Narayan, G., Mandel, K., ... Blondin, S. (2011). On the interpretation of supernova light echo profiles and spectra. *The Astrophysical Journal*, *732*(1), 2.

Rest, A., Sinnott, B., Welch, D. L., Prieto, J. L., Bianco, F. B., Matheson, T., ... Suntzeff, N. B. (2015). Light Echoes of Ancient Transients with the Blanco CTIO 4m Telescope. *arXiv preprint arXiv:1502.03705*.

Rest, A., Stubbs, C., Becker, A. C., Miknaitis, G. A., Miceli, A., Covarrubias, R., ... Olsen, K. (2005). Testing LMC microlensing scenarios: the discrimination power of the SuperMACHO microlensing survey. *The Astrophysical Journal*, *634*(2), 1103.

Rest, A., Suntzeff, N. B., Olsen, K., Prieto, J. L., Smith, R. C., Welch, D. L., ... Cook, K. (2005). Light echoes from ancient supernovae in the Large Magellanic Cloud. *Nature*, *438*(7071), 1132–1134.

Rest, A., Welch, D. L., Suntzeff, N. B., Oaster, L., Lanning, H., Olsen, K., ... Challis, P. (2008). Scattered-light echoes from the historical galactic supernovae Cassiopeia A and Tycho (SN 1572). *The Astrophysical Journal Letters*, *681*(2), L81.

Reynolds, S. P., Borkowski, K. J., Green, D. A., Hwang, U., Harrus, I., & Petre, R. (2008). The youngest galactic supernova remnant: G1. 9+ 0.3. *The Astrophysical Journal Letters*, *680*(1), L41.

Ritchey, G. W. (1901). Changes in the nebulosity about Nova Persei. *The Astrophysical Journal*, *14*, 293–294.

Roberts, T. P., & Colbert, E. J. M. (2003). Chandra reveals a black hole X-ray binary within the ultraluminous supernova remnant MF 16. *Monthly Notices of the Royal Astronomical Society*, *341*(4), L49–L54.

Scargle, J. D. (1989). Studies in astronomical time series analysis. III-Fourier transforms, autocorrelation functions, and cross-correlation functions of unevenly spaced data. *The Astrophysical Journal*, *343*, 874–887.

Schmidt, B. P., Kirshner, R. P., Leibundgut, B., Wells, L. A., Porter, A. C., Ruiz-Lapuente, P., ... Filippenko, A. V. (1994). SN 1991T: Reflections of past glory. *The Astrophysical Journal*, *434*, L19–L23.

Schweiker, H. (2015). *Currently Available Mosaic Filters.* Retrieved from `http://www.noao.edu/kpno/mosaic/filters/`

Schweiker, H., Howell, S., & Sawyer, D. (2011). *KPNO MOSAIC-1.1 IMAGER USER MANUAL.* Retrieved from `https://www.noao.edu/kpno/mosaic/manual/`

Sinnott, B. (2013). *Spectroscopy and Photometry of Scattered Light Echoes from Supernovae* (Unpublished doctoral dissertation).

Sinnott, B., Welch, D. L., Rest, A., Sutherland, P. G., & Bergmann, M. (2013). Asymmetry in the Outburst of SN 1987A Detected Using Light Echo Spectroscopy. *The Astrophysical Journal*, *767*(1), 45.

Smartt, S. J. (2009, sep). Progenitors of Core-Collapse Supernovae. *Annual Review of Astronomy and Astrophysics*, *47*(1), 63–106. doi: 10.1146/annurev-astro-082708-101737

Smartt, S. J., Eldridge, J. J., Crockett, R. M., & Maund, J. R. (2009). The death of massive stars–I. Observational constraints on the progenitors of Type II-P supernovae. *Monthly Notices of the Royal Astronomical Society*, *395*(3), 1409–1437.

Sparks, W. B., Macchetto, F., Panagia, N., Boffi, F. R., Branch, D., Hazen, M. L., & Della Valle, M. (1999). Evolution of the Light Echo of SN 1991TBased on observations with the NASA/ESA Hubble Space Telescope, which is operated by AURA, Inc., under NASA contract NAS 5-26555 and by STScI grant GO-06713.01-95A. *The Astrophysical Journal*, *523*(2), 585.

Stephenson, F. R., & Green, D. A. (2002). Historical supernovae and their remnants. *Historical supernovae and their remnants, by F. Richard Stephenson and David A. Green. International series in astronomy and astrophysics, vol. 5. Oxford: Clarendon Press, 2002, ISBN 0198507666*, *5*.

Strom, R. G. (1988). Distances to the remnants of historical Type I supernovae. *Monthly Notices of the Royal Astronomical Society*, *230*(2), 331–344.

Sugerman, B. E. K., Andrews, J. E., Barlow, M. J., Clayton, G. C., Ercolano, B., Ghavamian, P., ... Otsuka, M. (2012). Thirty years of SN 1980K: Evidence for light echoes. *The Astrophysical Journal*, *749*(2), 170.

Sugerman, B. E. K., & Crotts, A. P. S. (2002). Multiple light echoes from SN 1993J. *The Astrophysical Journal Letters*, *581*(2), L97.

Suntzeff, N. B., Heathcote, S., Weller, W. G., Caldwell, N., & Huchra, J. P. (1988). The light echoes from SN1987A. *Nature*, *334*, 135–138.

Tammann, G. A., Loeffler, W., & Schroeder, A. (1994). The Galactic supernova rate. *The Astrophysical Journal Supplement Series*, *92*, 487–493.

Tian, W. W., & Leahy, D. A. (2011). Tycho SN 1572: a naked Ia Supernova remnant without an associated ambient molecular cloud. *The Astrophysical Journal Letters*, *729*(2), L15.

Tonry, J., & Davis, M. (1979). A survey of galaxy redshifts. I-Data reduction techniques. *The Astronomical Journal*, *84*, 1511–1525.

Turatto, M. (2003). Classification of supernovae. In *Supernovae and gamma-ray bursters* (pp. 21–36). Springer.

Tylenda, R. (2004). On the light echo in V838 Mon. *Astronomy & Astrophysics*, *414*(1), 223–233.

Welch, D. L. (2014). Surveying for Historical Supernovae Light Echoes in the Milky Way Field. *Journal of the American Association of Variable Star Observers (JAAVSO)*, *42*, 473.

Wells, D., Greisen, E., & Harten, R. (1981). FITS: A flexible image transport system. *Astronomy & Astrophysics Supplement Series*, *44*, 363–370.

Whelan, J., & Iben Jr, I. (1973). Binaries and supernovae of type I. *The Astrophysical Journal*, *186*, 1007–1014.

Woosley, S. E. (1997). Neutron-rich nucleosynthesis in carbon deflagration supernovae. *The Astrophysical Journal*, *476*(2), 801.

Woosley, S. E. (2012). *Supernovae: The Tenth Santa Cruz Workshop in Astronomy and Astrophysics, July 9 to 21, 1989, Lick Observatory*. Springer Science & Business Media.

Zwicky, F. (1940). Types of novae. *Reviews of Modern Physics*, *12*(1), 66.